



AFRL-RX-WP-TR-2012-0349

ELECTROCHEMICAL ENERGY STORAGE MATERIALS

Michael F. Durstock, Benji Maruyama, and Patrick S. Carlin
Nanostructured and Biological Materials Branch
Nonmetallic Materials Division

Gyanaranjan Pattanaik, Jacob M. Haag, Daylond Hooper, and Gordon Sargent
UES Inc.

Placidus Amama and Neal A. Pierce
University of Dayton Research Institute

Rahul Rao
National Research Council

Kent Weaver
SOCHE Inc.

JULY 2012
Final Report

Approved for public release; distribution unlimited. Refer other requests for this document to AFRL/RXAS, Wright-Patterson Air Force Base, OH 45433-7750.

AIR FORCE RESEARCH LABORATORY
MATERIALS AND MANUFACTURING DIRECTORATE
WRIGHT-PATTERSON AIR FORCE BASE, OH 45433-7750
AIR FORCE MATERIEL COMMAND
UNITED STATES AIR FORCE

NOTICE AND SIGNATURE PAGE

Using Government drawings, specifications, or other data included in this document for any purpose other than Government procurement does not in any way obligate the U.S. Government. The fact that the Government formulated or supplied the drawings, specifications, or other data does not license the holder or any other person or corporation; or convey any rights or permission to manufacture, use, or sell any patented invention that may relate to them.

This report was cleared for public release by the USAF 88th Air Base Wing (88 ABW) Public Affairs Office (PAO) and is available to the general public, including foreign nationals.

Copies may be obtained from the Defense Technical Information Center (DTIC) (<http://www.dtic.mil>).

AFRL-RX-WP-TR-2012-0349 HAS BEEN REVIEWED AND IS APPROVED FOR PUBLICATION IN ACCORDANCE WITH ASSIGNED DISTRIBUTION STATEMENT.

//SIGNED//

PATRICK S. CARLIN, Program Manager
Soft Matter Materials Branch
Functional Materials Division

//SIGNED//

KATIE E. THORP, Acting Chief
Soft Matter Materials Branch
Functional Materials Division

//SIGNED//

KAREN R. OLSON, Deputy Chief
Functional Materials Division
Materials and Manufacturing Directorate

This report is published in the interest of scientific and technical information exchange, and its publication does not constitute the Government's approval or disapproval of its ideas or findings.

REPORT DOCUMENTATION PAGE				<i>Form Approved</i> OMB No. 0704-0188	
<p>The public reporting burden for this collection of information is estimated to average 1 hour per response, including the time for reviewing instructions, searching existing data sources, gathering and maintaining the data needed, and completing and reviewing the collection of information. Send comments regarding this burden estimate or any other aspect of this collection of information, including suggestions for reducing this burden, to Department of Defense, Washington Headquarters Services, Directorate for Information Operations and Reports (0704-0188), 1215 Jefferson Davis Highway, Suite 1204, Arlington, VA 22202-4302. Respondents should be aware that notwithstanding any other provision of law, no person shall be subject to any penalty for failing to comply with a collection of information if it does not display a currently valid OMB control number. PLEASE DO NOT RETURN YOUR FORM TO THE ABOVE ADDRESS.</p>					
1. REPORT DATE (DD-MM-YY) July 2012		2. REPORT TYPE Final		3. DATES COVERED (From - To) 01 Oct 2006 – 30 Sep 2011	
4. TITLE AND SUBTITLE ELECTROCHEMICAL ENERGY STORAGE MATERIALS				5a. CONTRACT NUMBER In-house	
				5b. GRANT NUMBER	
				5c. PROGRAM ELEMENT NUMBER 62102F	
6. AUTHOR(S) Michael F. Durstock, Benji Maruyama, and Patrick S. Carlin (RXAS) Gyanaranjan Pattanaik, Jacob M. Haag, Daylond Hooper, and Gordon Sargent (UES Inc.) Placidus Amama and Neal A. Pierce (University of Dayton Research Institute) Rahul Rao (National Research Council) Kent Weaver (SOCHE Inc.)				5d. PROJECT NUMBER 4347	
				5e. TASK NUMBER ML	
				5f. WORK UNIT NUMBER 12200002	
7. PERFORMING ORGANIZATION NAME(S) AND ADDRESS(ES) Nanostructured and Biological Materials Branch Nonmetallic Materials Division Air Force Research Laboratory, Materials and Manufacturing Directorate Wright-Patterson Air Force Base, OH 45433-7750 Air Force Materiel Command, United States Air Force				8. PERFORMING ORGANIZATION REPORT NUMBER AFRL-RX-WP-TR-2012-0349	
9. SPONSORING/MONITORING AGENCY NAME(S) AND ADDRESS(ES) Air Force Research Laboratory Materials and Manufacturing Directorate Wright-Patterson Air Force Base, OH 45433-7750 Air Force Materiel Command United States Air Force				10. SPONSORING/MONITORING AGENCY ACRONYM(S) AFRL/RXAS	
				11. SPONSORING/MONITORING AGENCY REPORT NUMBER(S) AFRL-RX-WP-TR-2012-0349	
12. DISTRIBUTION/AVAILABILITY STATEMENT Approved for public release; distribution unlimited.					
13. SUPPLEMENTARY NOTES The U.S. Government is joint author of this work and has the right to use, modify, reproduce, release, perform, display, or disclose the work. PA Case Number and clearance date: 88ABW-2012-3769, 5 July 2012. This document contains color.					
14. ABSTRACT The objective of the Electrochemical Energy Storage program is to develop enabling materials systems for future electrochemical energy storage devices. The program focuses on developing nanostructured electrodes and improved solid state electrolytes for high power & energy density devices and to explore new 3D nanostructured architectures to enable optimal performance. The goal is to supply performance improvement (i.e. increased power and energy density, longer shelf and use life, and higher charge/discharge rates) as well as provide new capabilities such as flexibility or the ability to incorporate energy storage directly into electronic devices, structures, or fabrics. Application focus for improved electrochemical energy storage materials is small autonomously powered remotely piloted aircraft (RPAs), airfield support, deployed airbase power, and portable soldier power. Near term goal is to increase energy density to allow 4-5X mission duration. Long term goal is to provide an autonomous power system by coupling improved energy storage with energy harvesting to permit 24/7 operation.					
15. SUBJECT TERMS Nanostructured Anodes & Cathodes, Solid State Electrolytes, 3D Nanostructured Battery Architectures, Nanostructured Lithium Ion Batteries					
16. SECURITY CLASSIFICATION OF:			17. LIMITATION OF ABSTRACT: SAR	18. NUMBER OF PAGES 40	19a. NAME OF RESPONSIBLE PERSON (Monitor) Patrick S. Carlin 19b. TELEPHONE NUMBER (Include Area Code) N/A
a. REPORT Unclassified	b. ABSTRACT Unclassified	c. THIS PAGE Unclassified			

TABLE OF CONTENTS

Section	Page
LIST OF FIGURES.....	ii
1 SUMMARY	1
2 NANOSTRUCTURED MATERIALS FOR ELECTROCHEMICAL ENERGY STORAGE DEVICES TASK	2
2.1 Research Objectives.....	2
2.2 Summary and Forecast for Future.....	2
2.3 Task Introduction.....	2
2.4 ALD Growth of TiO ₂	3
2.5 TiO ₂ Coated Ni Nanowire Arrays as Li-ion Battery Anodes	7
2.6 Solid Electrolyte Films by ALD	12
3 ARCHITECTURAL CONTROL OF NANOMATERIALS FOR STRUCTURAL BATTERIES	14
3.1 Research Objectives.....	14
3.2 Summary and Forecast for Future.....	14
3.3 Task Introduction	14
3.4 Low Temperature ALD of SnOx	15
3.5 High Temperature ALD of SnOx	18
3.6 SnOx Nanoparticle Coated Buckypaper 3D Electrodes	21
3.7 Electrochemical Performance of Conformal Growth vs. Nanoparticles	24
4 RELATED PUBLICATIONS.....	27
5 RECOMMENDATIONS.....	31
6 REFERENCES.....	32
7 LIST OF ACRONYMS AND SYMBOLS	34

LIST OF FIGURES

Figure 1. (A) Polystyrene sphere assembly with ALD deposited TiO ₂ layer around the spheres. (B) Interconnected TiO ₂ hollow spheres obtained after removing the PS template by annealing at 500 C for 3 h.	4
Figure 2. ALD TiO ₂ deposited onto anodic aluminum oxide template (one end closed) after template removal by etching in 1M NaOH. The open end of the pores lead to interconnected tubes (d) and the closed end of the pore lead to closed nanotubes (b,c).	5
Figure 3. ALD TiO ₂ deposited in commercial porous anodic aluminum oxide membranes (Anodisc 13) with open ends. After removing the deposit on one side with fine sand paper and etching the template with 1M NaOH the TiO ₂ nanotubes are revealed as shown above.	5
Figure 4. TEM bright field images of thin ~ 7nm (a, b) and thick ~25 nm (c) TiO ₂ nanotubes deposited in aluminum oxide templates.	6
Figure 5. TEM dark field and bright field images showing grain structure of thin (~5 nm) as-deposited ALD TiO ₂ nanotubes grown in aluminum oxide template.....	6
Figure 6. TEM dark field and bright field images showing grain structure of thick (~25 nm) annealed ALD TiO ₂ nanotubes grown in aluminum oxide template.....	6
Figure 7. Electrodeposited Cu nanotubes grown using PEG as a growth suppressor to yield nanotubular growth in nanoporous aluminum oxide template.....	7
Figure 8. Cross-section and top-view of electrodeposited Ni nanowire arrays, as 3D current collectors for Li-ion battery electrodes.	8
Figure 9. TiO ₂ deposited by ALD (~20 nm) on Ni Nanowires.	8
Figure 10. TEM bright field image confirming conformal growth of TiO ₂ on Ni nanowires (top left). EDS spectra confirms elemental composition of the ALD TiO ₂ layer. Selected area diffraction shows the deposit to be anatase TiO ₂ with a possible brookite fraction owing to the ring corresponding to d = 2.95 angstroms.	9
Figure 11. X-ray diffractograms of Ni nanowire substrate, as-deposited ALD TiO ₂ on Ni nanowires and annealed ALD TiO ₂ on Ni nanowires.	10
Figure 12. (A) Charge-discharge profiles of ALD TiO ₂ layer coated Ni nanowires electrodes annealed at 450 ^o C in Argon for 2 hours. (B) Comparative areal capacity of 3D TiO ₂ coated Ni nanowires and 2D TiO ₂ film electrodes.....	11
Fig 13. TEM bright field, dark field and selected area diffraction of ALD TiO ₂ coated Ni nanowire after 20 cycles of galvanostatic electrochemical charge-discharge.....	11
Figure 14. X-ray diffractograms of LiO _x /TiO _x deposited on MWCNT buckypapers by ALD after annealing at 550 ^o C for 3h (red) and 800 ^o C for 4h (black).	12
Figure 15. As-deposited (top) and annealed (bottom) LiO _x /TiO _x multilayers grown by ALD on MWCNT buckypaper.	13
Figure 16. Electrochemical charge-discharge profiles and capacity values as a function of cycle number for LiO _x /TiO _x ALD deposits on Ni nanowire array electrode.....	13

Figure 17. TEM images of (a) CNT coated with 100 LT-ALD cycles of SnOx and (b) CNT coated with 300 LT-ALD cycles of SnOx..... 16

Figure 18. XRD patterns of CNTs, CNTs coated with 100 LT-ALD SnOx cycles, and CNTs coated with 300 LT-ALD SnOx cycles. 17

Figure 19. XRD patterns of LT-ALD as deposited SnOx on CNTs and annealed SnOx on CNTs..... 17

Figure 20. SEM images of (a) MW-CNT Buckypaper and SnOx coated Buckypaper after (b) 50, (c) 100, (d) 300, (e) 500 TDMASn-H2O HT-ALD cycles. 18

Figure 21. (a) XRD patterns of Buckypaper and SnOx deposited on Buckypaper after (b) 50, (c) 100, (d) 300, (e) 500 TDMASn-H2O HT-ALD cycles (b) a representative EDX spectra of Buckypaper coated with 300 SnOx HT-ALD cycles. 19

Figure 22. Cross sectional SEM images of SnOx coated Buckypaper after 100 and 500 HT-ALD cycles. 20

Figure 23. XRD patterns of Buckypaper, HT-ALD as deposited SnOx on Buckypaper, and HT-ALD annealed SnOx on Buckypaper. 21

Figure 24. (a) Charge-discharge curves of Buckypaper and (b) charge-discharge curves of Buckypaper coated with 300 SnOx HT-ALD cycles cycled against Li. 22

Figure 25. (a) Specific capacity of the Buckypaper and SnOx coated Buckypaper with different number of HT-ALD cycles (b) Specific capacity of the SnOx component of the HT-ALD SnOx coated Buckypaper. 23

Figure 26. Areal charge and discharge capacities of Buckypaper coated with 300 SnOx HT-ALD cycles..... 24

Figure 27. (a) LT-ALD of SnOx on Buckypaper (b) HT-ALD of SnOx on Buckypaper. 25

Figure 28. Specific capacity and coulombic efficiency of Buckypaper coated with 100 SnOx ALD cycles. The squares correspond with the specific capacity and the circles with the coulombic efficiency..... 25

Figure 29. Specific capacity and coulombic efficiency of Buckypaper coated with 300 SnOx ALD cycles. The squares correspond with the specific capacity and the circles with the coulombic efficiency..... 26

1 SUMMARY

The objective of the Electrochemical Energy Storage program is to develop enabling materials systems for future electrochemical energy storage devices. The program focuses on developing nanostructured electrodes and improved solid state electrolytes for high power & energy density devices and to explore new 3D nanostructured architectures to enable optimal performance. The goal is to supply performance improvement (i.e. increased power and energy density, longer shelf and use life, and higher charge/discharge rates) as well as provide new capabilities such as flexibility or the ability to incorporate energy storage directly into electronic devices, structures, or fabrics. Application focus for improved electrochemical energy storage materials is small autonomously powered remote piloted aircraft (RPAs), airfield support, deployed airbase power, and portable soldier power. The near term program goal is to increase energy density to allow 4-5X mission duration. The long term program goal is to provide an autonomous power system by coupling improved energy storage with energy harvesting to permit 24/7 operation.

This in-house research program consisted of 2 separate AFOSR sponsored tasks: Nanostructured Materials for Electrochemical Energy Storage Devices (Sponsored by Dr. Charles Lee, AFOSR/NL) and Architectural Control of Nanomaterials for Structural Batteries (Sponsored by Dr. Les Lee, AFOSR/NL) and was supplemented with Materials and Manufacturing funding covering Government salary, supplies, and equipment.

This report is broken into the 2 AFOSR sponsored tasks and includes an appendix of publications and presentations providing more in depth technical detail of the program.

2 NANOSTRUCTURED MATERIALS FOR ELECTROCHEMICAL ENERGY STORAGE DEVICES TASK

2.1 Research Objectives

The research described in this report is comprised of the following two technical objectives:

- Nanostructured Battery Electrodes
- Solid Electrolyte Films by ALD

This task is focused on developing fundamental relationships between nanoscale structure and macroscopic properties of energy storage devices including battery electrodes and polymer electrolytes. A variety of approaches are being investigated to fabricate well controlled architectures of nanostructured electrodes with the goal of providing how this structure impacts both energy density and power density. In addition, new polymer electrolyte materials are being synthesized and characterized with the goal of improving proton conductivity, durability, and high temperature performance.

2.2 Summary and Forecast for Future

This task focuses on understanding the relationship between electrochemical behavior and nanoscale morphological control of lithium-ion battery electrode and electrolyte materials. We have explored a variety of ways to fabricate active electrode materials either as nanostructured arrays of the active materials, or as coatings on nanostructured arrays of current collectors. Atomic layer deposition (ALD) is used to conformally coat 3D current collector nanoarchitectures with nanometer scale control over the active layer thickness. This allows lithium ion diffusion in active electrode material that is limited to couple of nanometers, thereby facilitating high power devices. TiO_2 layers were deposited as an anode material on a variety of templates including porous anodic aluminum oxide, nickel and copper nanowire arrays, multi-walled carbon nanotube (CNT) buckypapers, vertically aligned CNTs, polystyrene sphere assemblies, and nickel nanospheres. In each case, highly uniform films with nanometer scale resolution were achieved and are being investigated for their performance in active devices. Specifically for the case of the TiO_2 coated nickel nanowire arrays, detailed morphological and electrochemical studies were carried out to demonstrate the utility of hybrid, 3D electrode architectures. Excitingly, a 2 order-of-magnitude increase in the areal capacity is observed for the 3D nanostructured electrodes when compared to their 2D analogues. In addition, we are extending this technique to deposit 3D, conformal solid electrolyte materials. Specifically, we are targeting the Li-La-Ti-O system since it has been demonstrated to have an ionic conductivity up to $1.0 \times 10^{-3} \text{ S cm}^{-1}$. We began with the Li-Ti-O system to demonstrate proof-of-concept and we have successfully deposited conformal layers that are comprised of a 2-phase network of TiO_2 and $\text{Li}_4\text{Ti}_5\text{O}_{12}$. The electrochemical characteristics of this material are such that it does not show a crystalline phase specific plateau at any voltage, but rather exhibits the constant formation of solid solution as Li-insertion proceeds. During the first 10 cycles, the charge and discharge capacities show excellent stability and we are now proceeding to deposit the full Li-La-Ti-O system.

2.3 Task Introduction

One of the most important requirements in next generation batteries is to concurrently deliver high energy density and high power density (fast charge-discharge rates). The high power density requirement can be met with enhanced ion and electron transport kinetics in batteries, which in turn requires active materials with high ion diffusion constants and conductive additives or architectures for faster electron transport to respective current collectors. It is well known that nanostructuring the electrode materials would

significantly enhance the characteristic time constant for ion diffusion ($t = L^2/D$, L: diffusion length and D: diffusion constant) thereby reducing the intercalation / deintercalation time [1]. However, nanostructuring electrode materials leads to some issues as well – such as, reduced electron transport kinetics through interparticle boundaries, and undesired side reactions due to high electrode/electrolyte surface area. In our nanostructured electrode materials studies we have chosen three-dimensional (3D) conducting nanoarchitected current collectors [2] (e.g., electrodeposited Ni nanowire arrays) and coating those with ultrathin conformal layers of active materials to circumvent the reduced electron transport kinetics issue. To get around the side reactions due to high electrode/electrolyte surface area, active materials and electrolytes may be suitably chosen which are least reactive, such as TiO_2 which is not known to form a solid electrolyte interphase (SEI) [3-4].

We have chosen atomic layer deposition (ALD) as a process to conformally coat the 3D current collector nanoarchitecture with nanometer scale control over active layer thickness. Thus the Li ion diffusion in active electrode material is limited to couple of nanometers and electron conducting current collector is in contact with the ultrathin active layer everywhere. Such 3D designs can enable us to achieve our ultimate goal of 3D all-solid-state microbatteries [5] by sequentially assembling an anode (cathode) layer followed by a solid electrolyte/separator and then the complementary cathode (anode) filling the space in between the nanowires. All solid-state 3D microbatteries will be crucial to successful operation of many miniaturized autonomous devices with significant interest to future USAF needs.

2.4 ALD Growth of TiO_2

TiO_2 films were deposited in a Savannah S100 ALD system (Cambridge NanoTech, Cambridge, USA) using tetrakis-dimethylamino titanium TDMAT (Strem Chemicals) and H_2O as precursors at 200 °C. High purity (99.9995%) N_2 was used as the carrier gas and typically 20 sccm of N_2 was used during deposition. The TiO_2 film deposition was carried out in the exposure mode using the stop valve feature of the equipment allowing higher diffusion time of precursor gas over the high aspect ratio nanopores/wires. TDMAT was pulsed for 0.2 s with 10 – 15 s purge (wait) time and H_2O was pulsed for 0.01 s with 5 – 8 s purge time in stop valve mode. The N_2 flow was reduced to 5 – 10 sccm during the stop valve mode to avoid overpressure limit. After each pulse of the precursor the stop valve is opened and the flow is changed back to 20 sccm and a purge time of 30 – 45 sec was allowed again for the self-limiting surface reaction as well as to remove any excessive precursors from the surface.

TiO_2 layers could be deposited on a variety of templates including porous anodic aluminum oxide, aluminum oxide template-assisted electrodeposited Ni nanowires and Cu nanotubes, multi-walled carbon nanotube (CNT) buckypapers, vertically aligned CNTs, polystyrene sphere assemblies, polystyrene spheres (PS) – assisted electrodeposited interconnected Ni nanospheres etc.

Polystyrene spheres: PS spheres (Thermo Scientific, 650 nm) were drop-casted from a diluted aqueous solution (2-10%) on a circular region defined by a punched Kapton tape and dried at 50 °C. Then the sample was further heat treated at 90 °C, right below its glass transition temperature. Then ALD deposition of TiO_2 was carried out on the PS sample filling the hollow space in between the PS spheres and around them. The PS spheres were then removed by annealing the sample at 500 °C for 3h (Figure 1) to obtain interconnected hollow spheres of TiO_2 with tunable thickness. The diameter of the hollow spheres can be controlled by using PS of various diameters.

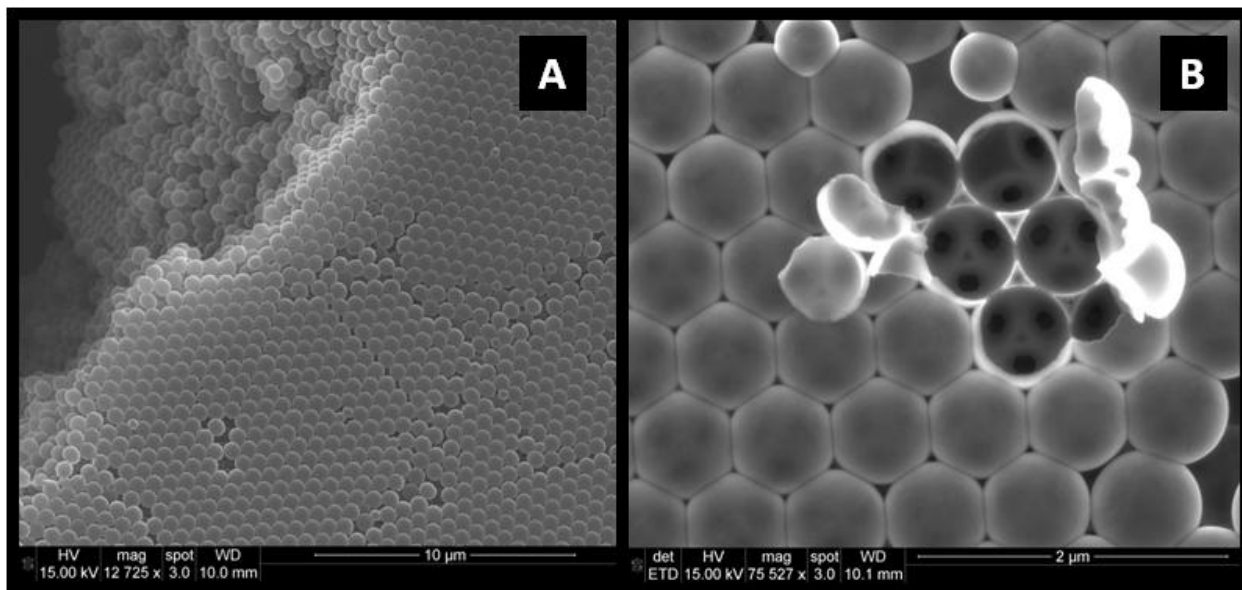


Figure 1. (A) Polystyrene sphere assembly with ALD deposited TiO₂ layer around the spheres. (B) Interconnected TiO₂ hollow spheres obtained after removing the PS template by annealing at 500 C for 3 h.

Aluminum oxide templates: Nanoporous aluminum oxide templates were used to deposit TiO₂ nanostructures through conformal deposition along the walls of the template by ALD. The nanopores fill uniformly on the walls of high-aspect ratio features resulting in TiO₂ nanotubes with tunable thickness as well as length. The thickness of the TiO₂ nanotubes can be precisely controlled at nanometer level with the number of ALD cycles and the length of the nanotubes through the anodization time. Conformal deposition could also be achieved in alumina templates with either only one end open or through-hole membranes. Figure 2 and 3 show SEM images of TiO₂ nanotubes grown on respective templates, after etching the aluminum oxide templates in NaOH solution. The ALD deposited nanotubes seem to be far denser than their sol-gel counterparts. This leads to the top-down etching of aluminum oxide template in ALD TiO₂ deposits on aluminum oxide templates rather than through pore-widening as in the case of sol-gel derived TiO₂ nanotubes. The dense ALD TiO₂ layer should help reduce grain boundaries resulting in reduced resistance to electronic conduction. Figure 4 shows their TEM images confirming conformal deposition in the high-aspect ratio nanopores. EDS spectra and selected area diffraction further confirmed the TiO₂ elemental composition and crystal phase, respectively. Grain structure of thinner as-deposited (< 8 nm) and thicker (> 20 nm) annealed TiO₂ nanotubes are shown in Figure 5 and 6, respectively. The as-deposited tubes have relatively large grain structures. The figures also further confirm dense pinhole-free deposits by ALD.

Carbon nanotubes: MWCNT buckypapers and vertically aligned carbon nanotubes (VACNT) have also been successfully used as templates to grow TiO₂ nanotubes by ALD. TiO₂ deposits seem to grow layer-by-layer on carbon nanotube surfaces, as observed by SEM and TEM. These templates have been extensively used for ALD deposition of SnO_x and also for Li-Ti-O system (section 3).

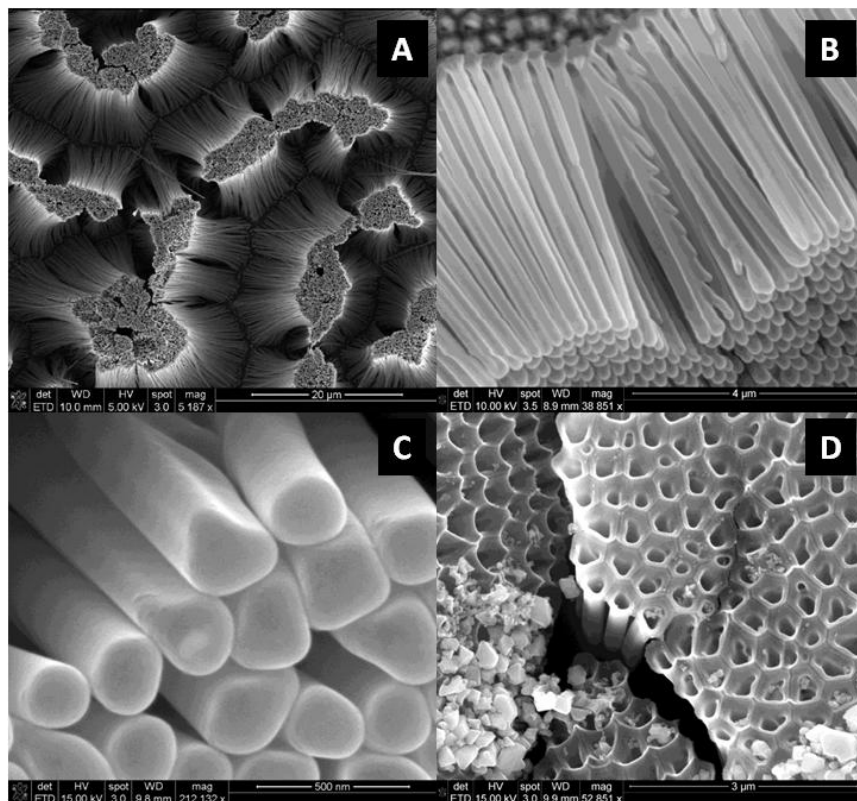


Figure 2. ALD TiO₂ deposited onto anodic aluminum oxide template (one end closed) after template removal by etching in 1M NaOH. The open end of the pores lead to interconnected tubes (d) and the closed end of the pore lead to closed nanotubes (b,c).

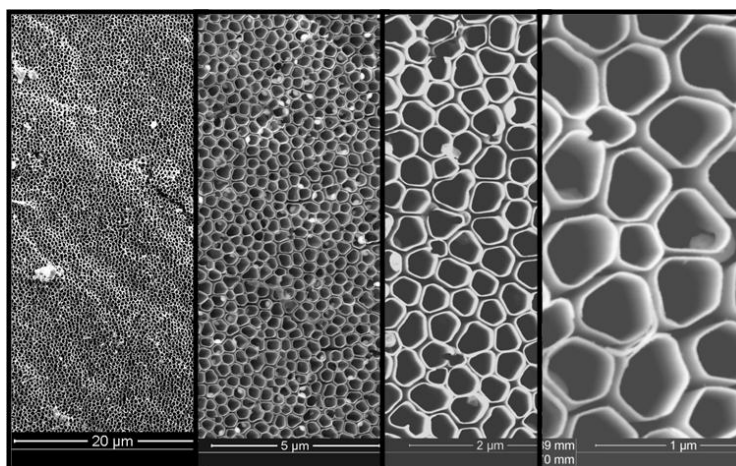


Figure 3. ALD TiO₂ deposited in commercial porous anodic aluminum oxide membranes (Anodisc 13) with open ends. After removing the deposit on one side with fine sand paper and etching the template with 1M NaOH the TiO₂ nanotubes are revealed as shown above.

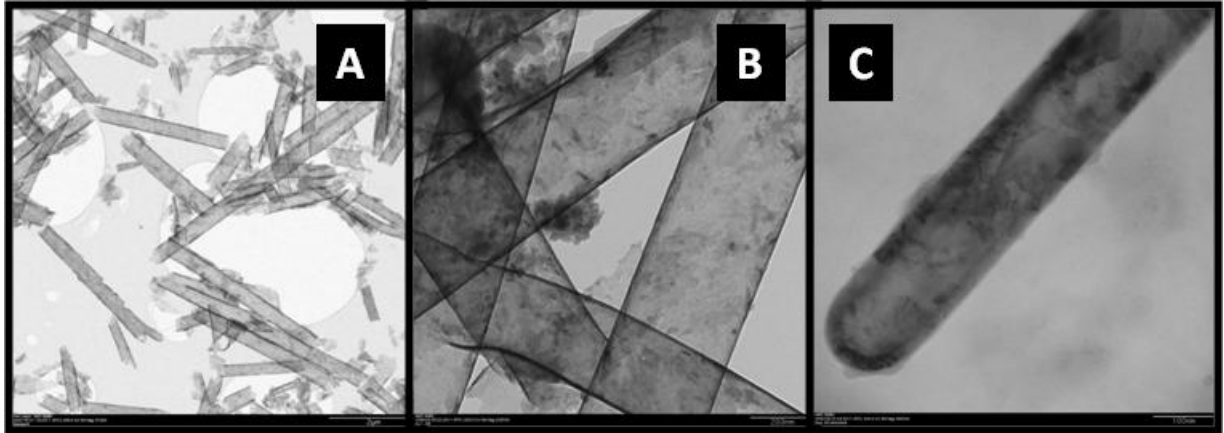


Figure 4. TEM bright field images of thin ~ 7 nm (a, b) and thick ~ 25 nm (c) TiO_2 nanotubes deposited in aluminum oxide templates.

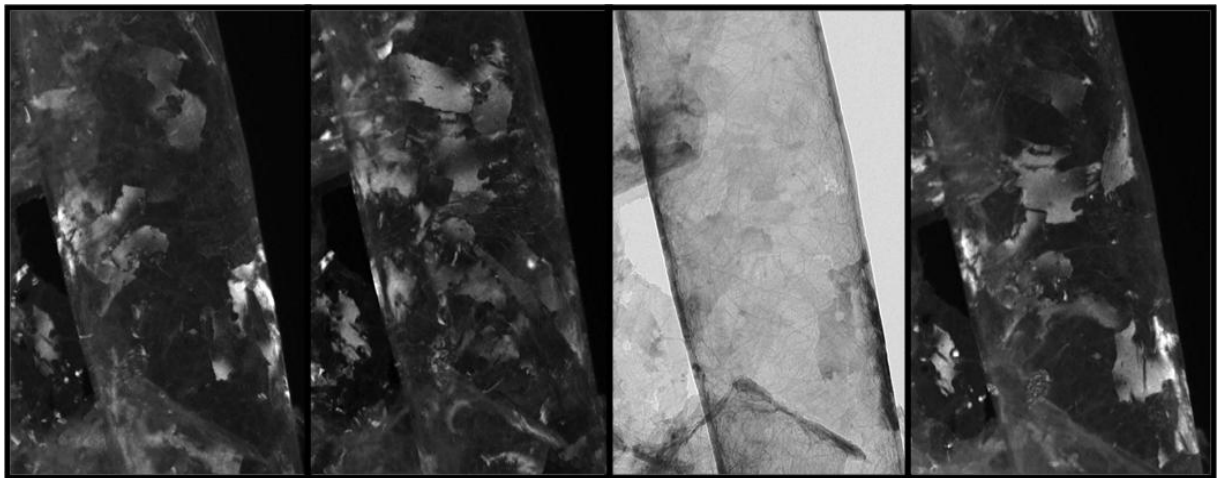


Figure 5. TEM dark field and bright field images showing grain structure of thin (~ 5 nm) as-deposited ALD TiO_2 nanotubes grown in aluminum oxide template.

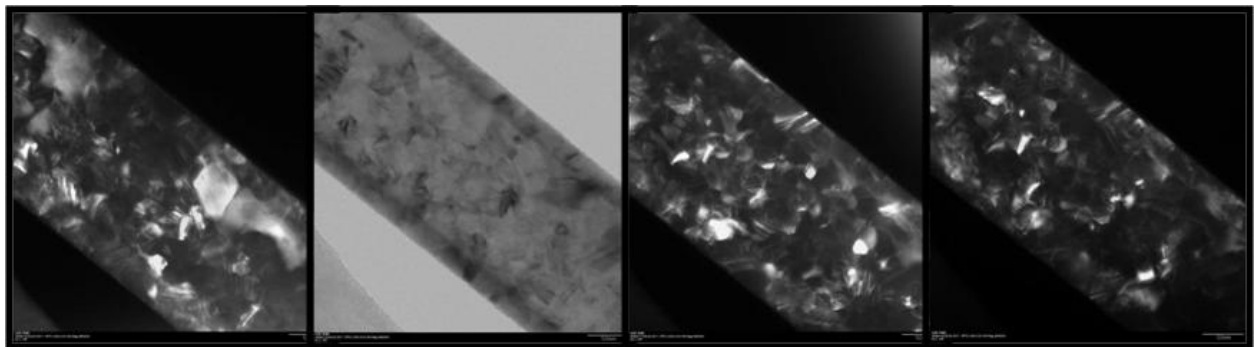


Figure 6. TEM dark field and bright field images showing grain structure of thick (~ 25 nm) annealed ALD TiO_2 nanotubes grown in aluminum oxide template.

Metal nanowires: Nickel nanowires have been deposited using aluminum oxide templates. The process for Ni nanowire growth and subsequent ALD TiO₂ deposition is discussed in detail in the following section. In a similar fashion, copper nanowires and also copper nanotubes (figure 7) have been electrodeposited as 3D current collectors. The nanotubes could be grown by suppressing the Cu electrodeposition in the pores using PEG and using relatively slow electrodeposition rates. ALD TiO₂ has been successfully deposited as conformal layers on these 3D metal nanostructure arrays.

Crystal structure of the ALD deposited TiO₂ nanotubes were studied using XRD. The as-deposited TiO₂ film on glass, CNTs and aluminum oxide membranes are amorphous, where as that on Ni nanowires are already crystallized to the anatase phase of TiO₂. However, post ALD thermal annealing could yield the desired anatase or rutile phase of TiO₂ on any of the templates.

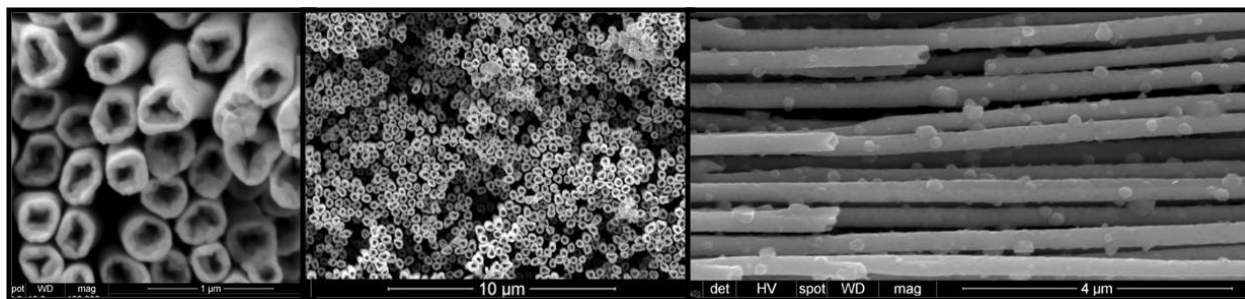


Figure 7. Electrodeposited Cu nanotubes grown using PEG as a growth suppressor to yield nanotubular growth in nanoporous aluminum oxide template.

2.5 TiO₂ Coated Ni Nanowire Arrays as Li-ion Battery Anodes

Electrodeposited Ni nanowire arrays: Ni nanowires were obtained by through-hole electrodeposition of Ni in porous anodic aluminum oxide membranes PAAMs (Whatman Anodisc 13, 60 μm thick, average pore diameter 200nm). The PAAMs were coated on one side with a Ni or Cu thin film by evaporation. A thicker Ni film (>10 μm) was then electrodeposited onto the evaporated film to provide a sturdy support. The pores were then filled with Ni nanowires by potentiostatic electrodeposition in a Watts bath using a PAR EG&G 263A potentiostat. Ni nanowire-filled PAAMs were thoroughly rinsed in deionized (DI) water and dried using a stream of N₂ gas. The aluminum oxide template was etched away using 1 M NaOH solution. The samples were then thoroughly rinsed in DI water and dried in a stream of N₂ gas or using supercritical drying with a liquid CO₂ critical point drier (CPD 7501, Fisons Instruments). About 30 μm long Ni nanowires were electrodeposited into the pores of aluminum oxide template for this study. The diameter of the Ni nanowires was in the range 200 – 300 nm. Figure 8 a and b show the SEM images of as prepared Ni nanowires on the Ni film support. These vertically aligned Ni nanowire arrays served as the 3D nanoarchitected current collectors.

TiO₂ deposition by ALD: The Ni nanowire substrates were dried in a vacuum oven at 160 °C and their mass was measured with a 6-digit balance before and after TiO₂ deposition. To make sure ALD TiO₂ does not deposit on the bottom side of the Ni support film, the sample was gently pressed on to a Kapton tape, with the Ni film in contact with the tape. The TiO₂ film deposition was carried out in the exposure mode using the stop valve feature of the equipment allowing higher diffusion time of precursor gas over the high aspect ratio Ni nanowire arrays.

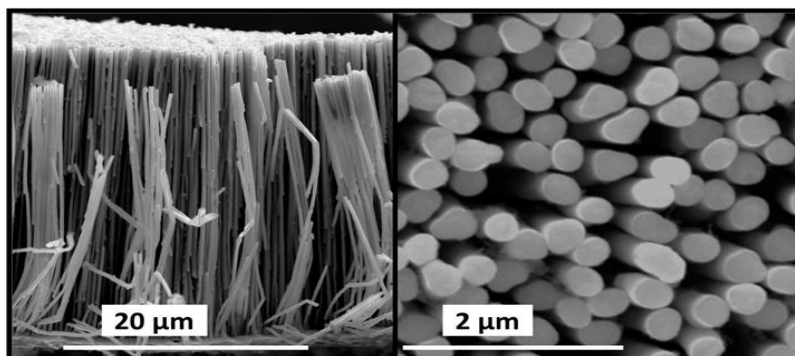


Figure 8. Cross-section and top-view of electrodeposited Ni nanowire arrays, as 3D current collectors for Li-ion battery electrodes.

Figure 9 shows SEM images of Ni nanowires after 500 ALD cycles of TiO_2 deposition. In Figure 9a, the top view of the nanowire array, the contour around the nanowire shows an impression of the ALD TiO_2 layer on nanowires. Both the top-view and the cross-sectional view (Figure 9b) SEM images of the sample indicate the TiO_2 deposited nanowires are well separated to allow the electrolyte diffusion in an electrochemical cell. Figure 9c shows a zoomed cross-sectional view of the TiO_2 coated Ni nanowires where an impression of the conformal TiO_2 layer along the length of the nanowire could be noticed. Further confirmation of conformal TiO_2 deposition all around the Ni nanowire can be seen in Figure 9d-f. Since the cross-sectional sample was prepared by cutting the sample with a pair of scissors, some nanowires are stretched or bent. The metallic Ni nanowire is malleable and easily stretched or bent. However, the TiO_2 layer is fractured in the process. Some of these stretched (Figure 9d) and bent (Figure 9e & f) nanowires clearly show the conformal deposition of ALD TiO_2 .

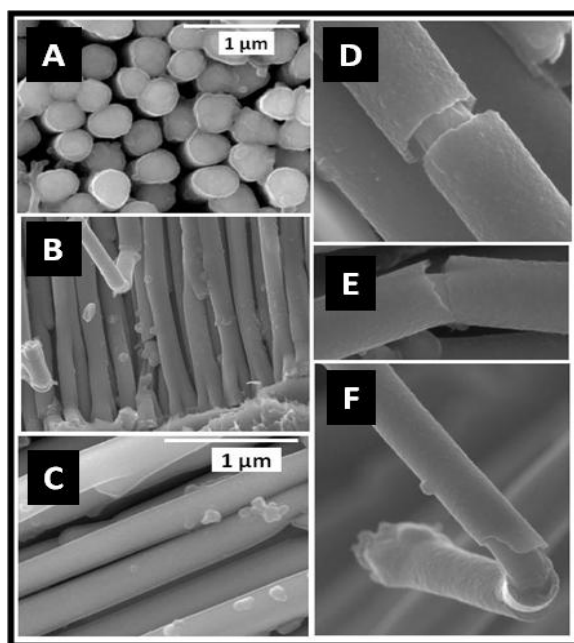


Figure 9. TiO_2 deposited by ALD (~20 nm) on Ni Nanowires.

TEM studies were carried out to further confirm the conformal deposition of TiO₂ on Ni nanowires and to investigate their crystal structure and local elemental composition. Figure 10a shows a representative bright field TEM image of a Ni nanowire coated with 500 ALD cycles of TiO₂ and annealed in Argon at 450°C for 2 h. TEM confirms conformal growth of TiO₂ all over the Ni nanowires as shown in the figure with a representative image. The thickness of the TiO₂ layer on Ni nanowires is 20 ± 2 nm for 500 ALD cycles, implying the deposition rate to be about 0.04 nm per cycle. EDS spectra were collected in TEM for qualitative examination of elemental composition. Figure 10b shows a representative EDS spectra collected primarily from the ALD layer with the aperture focused on it. EDS confirms TiO_x deposition showing Ti and O peaks, along with Ni peaks from the core nanowire. To determine the crystallinity of the TiO_x layer, selected area diffraction (SAD) in TEM was performed. Figure 10c shows a SAD pattern collected using the smallest spot size focused mostly on the TiO_x layer. The SAD pattern shows the signature of a polycrystalline deposit and the broken lines are due to the fact that only a few grains were covered in the SAD aperture. The lattice spacing, d-values, estimated from the diameter of the rings are noted on the image. Comparing to the standard data the ALD deposits seem to be primarily anatase TiO₂ (JCPDS PDF#21-1272) with a possible brookite fraction owing to the estimated d-value for the second innermost ring 2.95 which could be d₁₂₁ of brookite TiO₂ (JCPDS PDF#29-1360).

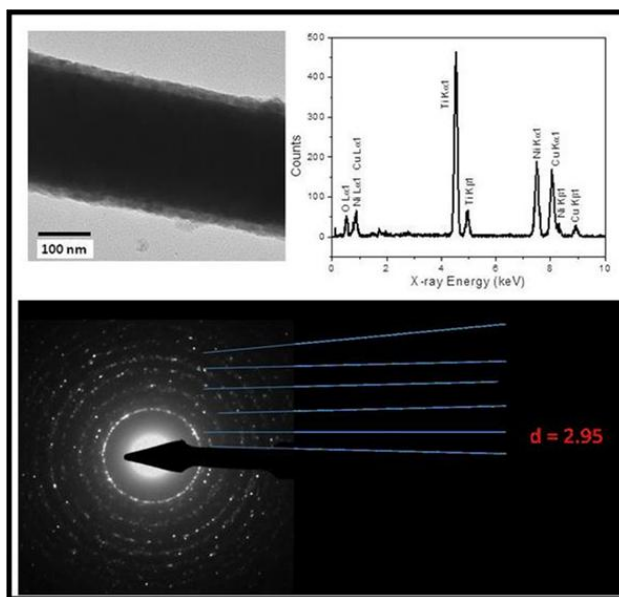


Figure 10. TEM bright field image confirming conformal growth of TiO₂ on Ni nanowires (top left). EDS spectra confirms elemental composition of the ALD TiO₂ layer. Selected area diffraction shows the deposit to be anatase TiO₂ with a possible brookite fraction owing to the ring corresponding to d = 2.95 angstroms.

The crystal structure of the as-deposited and annealed ALD TiO₂ films on Ni nanowires were examined by XRD. Figure 11 shows X-ray diffractograms collected for (a) a bare Ni nanowire array substrate prior to TiO₂ deposition, (b) an as-deposited ALD TiO₂ film on Ni nanowires and (c) an ALD TiO₂ coated Ni nanowire sample annealed at 450 C for 2h in Ar. The samples were mounted on a small piece of glass slide using double sided scotch tape for XRD measurements. Hence an amorphous hump seen at lower angle is likely due to the glass slide. X-ray diffractogram for the as-deposited ALD TiO₂ coating on Ni nanowires shows the signature of an anatase phase, although an amorphous fraction in the deposit seems likely. In order to increase the crystalline phase fraction in the TiO₂ coating and also to remove any remnant precursor compounds in the deposit, the as-deposited sample was annealed at 450°C for 2h in Argon flow. XRD of annealed sample shows an increase in peak intensities indicating further enhancing

anatase phase formation. This might also indicate presence of an amorphous fraction in the as-deposited ALD TiO₂ coating. The appearance of a peak at 30.9° in the XRD spectrum for the annealed sample with a d-value 0.29 nm indicates a small Brookite phase in the TiO₂ coating (JCPDS PDF#29-1360), which can be ascribed to the (121) plane. The XRD data is in agreement with TEM results confirming mostly anatase phase of the ALD TiO₂ coating.

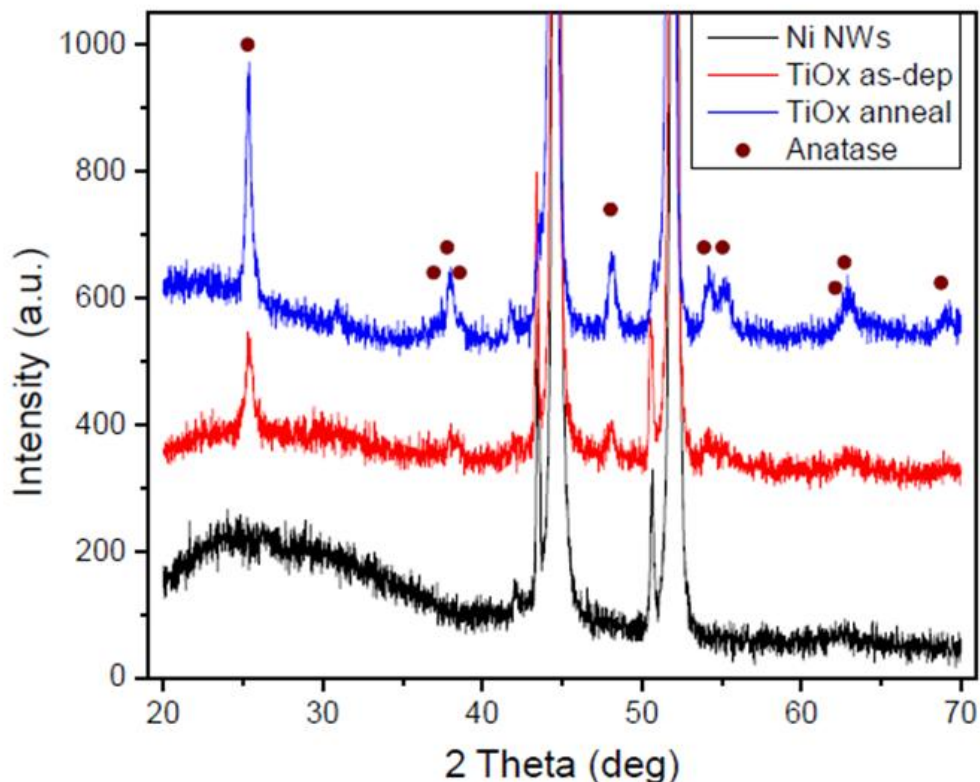


Figure 11. X-ray diffractograms of Ni nanowire substrate, as-deposited ALD TiO₂ on Ni nanowires and annealed ALD TiO₂ on Ni nanowires.

Electrochemical characterization was carried out in an argon filled glove box with a two-electrode Swagelok® test cell using a Maccor 4300 battery testing system. Electrochemical half-cells were assembled using the TiO₂ coated Ni nanowire arrays (working electrode) and Li foil (counter electrode) separated by two layers of porous polypropylene membrane (Celgrad® 2400) separators soaked in a liquid electrolyte solution containing 1.0 M lithium hexafluorophosphate (LiPF₆) in 1:1 ethylene carbonate (EC)/diethyl carbonate (DEC) solution. The charge-discharge profiles for the 1st, 2nd, 5th, 10th and 20th cycles at a scan rate of 16.5 mA/g (constant current) are shown in Figure 12a. There is a large irreversible capacity observed between the 1st and 2nd discharge. This is believed to be due to the presence of remnant moistures in the electrode or reduction of the oxidized Ni current collectors. The discharge capacity after second cycle seems to stabilize well for a value of about 180 mAh/g. The discharge capacity is always a little higher than that for the corresponding charge cycle. This could mean some of the intercalated Li ions are lost to some irreversible process and not released during the de-insertion (charge) process. There is a marginal increase in charge capacity from 1st to 20th cycle indicating the process is stabilizing. The discharge curve shows a plateau at a potential between 1.7 – 1.8

V. This plateau has been ascribed to Li insertion potential for anatase TiO₂. However, this does not constitute for the entire discharge process. There is also a significant fraction of the discharge capacity owing to the gradual solid-solution like process indicating presence of amorphous fraction in the ALD TiO₂ coating in the sample. This amorphous phase might be contributing to the difference in charge and discharge capacities. Figure 12b shows the comparison of the areal capacities of the ALD TiO₂ on 3D nanowire array electrode and a 2D thin film. There is about 2 orders of magnitude increase in the areal capacities making these 3D electrodes suitable for microbatteries.

Figure 13 shows TEM studies on an electrochemically cycled ALD TiO₂ coated Ni nanowire sample. The bright and dark field images show the film the TiO₂ layer to be stable after 20 cycles. Selected area diffraction is not able to discern any significant crystal structure change after 20 cycles of charge-discharge.

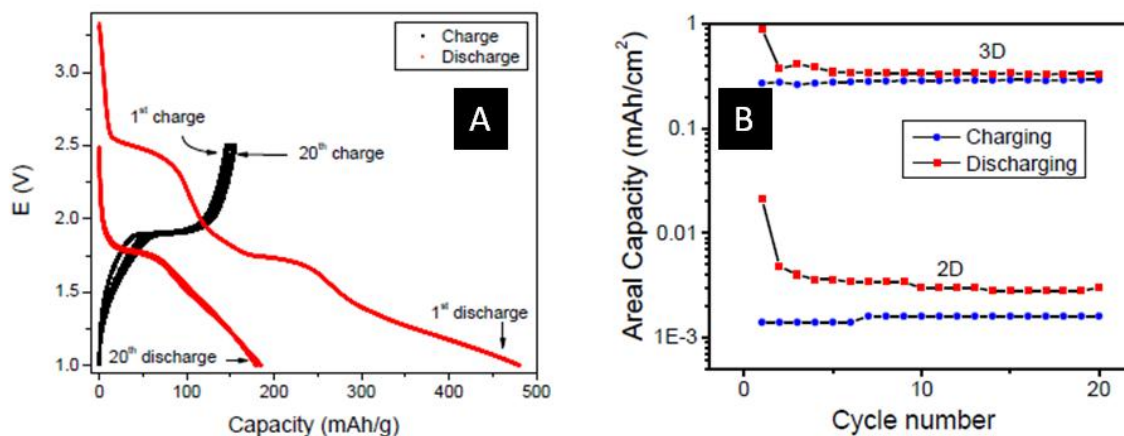


Figure 12. (A) Charge-discharge profiles of ALD TiO₂ layer coated Ni nanowires electrodes annealed at 450°C in Argon for 2 hours. (B) Comparative areal capacity of 3D TiO₂ coated Ni nanowires and 2D TiO₂ film electrodes.

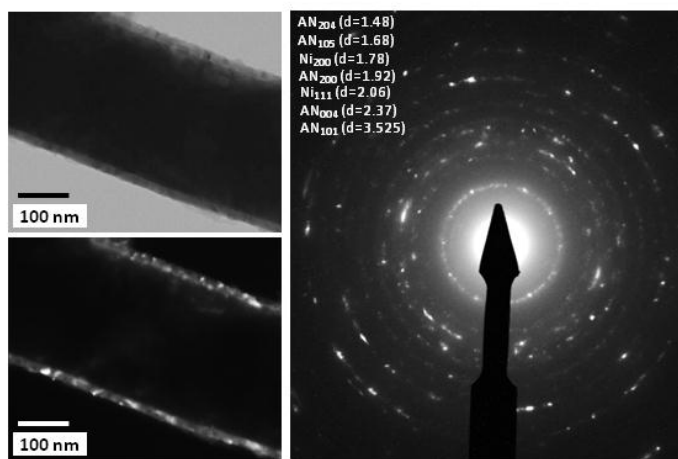


Fig 13. TEM bright field, dark field and selected area diffraction of ALD TiO₂ coated Ni nanowire after 20 cycles of galvanostatic electrochemical charge-discharge.

2.6 Solid Electrolyte Films by ALD

All-solid-state batteries have definitive advantages over their liquid electrolyte counterparts in safety, miniaturization and several applications including USAF interest-specific high altitude applications. 3D nanoelectrodes as discussed earlier could heavily benefit by use of conformal solid electrolyte layer on the 3D electrode architecture in designing 3D microbatteries. With this motivation we plan to grow ceramic Li-La-Ti-O as a possible solid electrolyte materials as it can have ionic conductivity values up to $1.0 \times 10^{-3} \text{ S cm}^{-1}$ [6]. Before growing the ternary system we first attempted to grow the binary Li-Ti-Ox film by ALD. We used the recipe for TiOx and a similar recipe for LiOx using water as a precursor and cycled alternately to deposit LiOx/TiOx bilayer system repeating for the desired thickness. To verify their crystal phase we carried out XRD studies. We observed the as-deposited film on buckypaper to be amorphous. After annealing at 550°C for about 3 hours the deposits still retain their CNT-like tubular shape. XRD showed the coexistence of two distinct phases – an anatase TiO₂ and a Li₄Ti₅O₁₂ phase. Subsequent annealing at 800°C resulted in a mostly rutile TiO₂ phase in combination with a Li₄Ti₅O₁₂ phase. However, such high temperature annealing in air leads to complete removal of carbon nanotubes and grain growth. X-ray diffractograms of the annealed samples are shown in Figure 14. Figure 15 shows SEM images of the as-deposited and annealed LiOx/TiOx films on Buckypaper. Such phase formation of TiO₂ and Li₄Ti₅O₁₂ has also been recently reported for sol-gel derived nanopowders from Li₂O and TiO₂ powders (Mohammadi, Fray, J. Sol-Gel Sci Tech 55, 19 (2010)). An as-deposited LiOx/TiOx sample on Ni nanowires was cycled in electrochemical workstation. The charge discharge curves are shown in Figure 16. It does not show a crystalline phase specific plateau at any voltage rather constant formation of solid solution as Li-insertion proceeds. During the first 10 cycles the charge and discharge capacities show excellent stability. We are proceeding to deposit Li-La-Ti-O system by ALD soon.

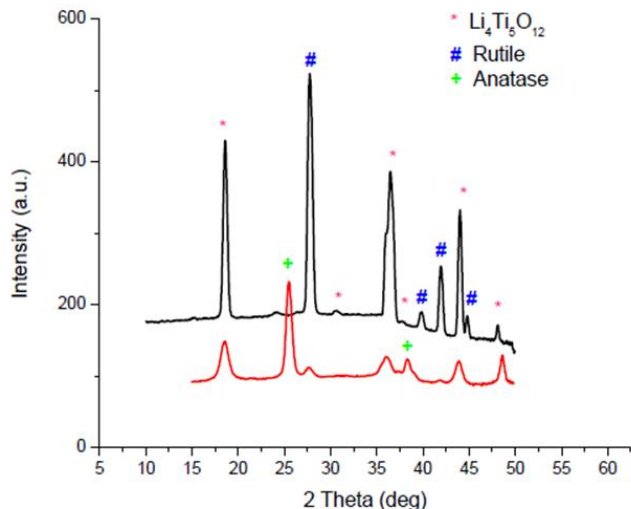


Figure 14. X-ray diffractograms of LiOx/TiOx deposited on MWCNT buckypapers by ALD after annealing at 550°C for 3h (red) and 800°C for 4h (black).

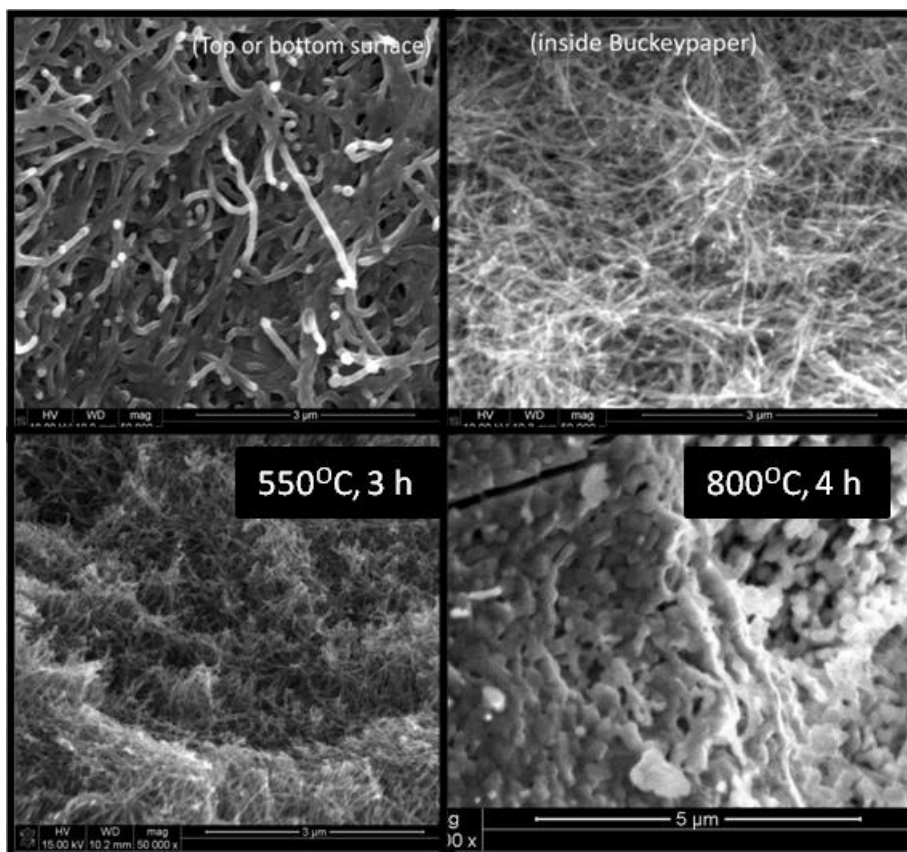


Figure 15. As-deposited (top) and annealed (bottom) LiOx/TiOx multilayers grown by ALD on MWCNT buckypaper.

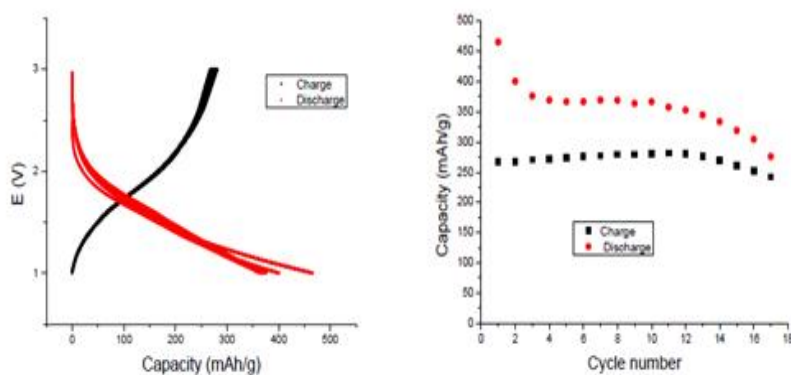


Figure 16. Electrochemical charge-discharge profiles and capacity values as a function of cycle number for LiOx/TiOx ALD deposits on Ni nanowire array electrode.

3 ARCHITECTURAL CONTROL OF NANOMATERIALS FOR STRUCTURAL BATTERIES

3.1 Research Objectives

The research described in this report is focused on developing the fabrication methodologies needed to create complex structures for use in 3D nanostructured batteries and establishing structure-property relationships correlating materials and device structure to electrical and mechanical performance. The aim of the research is to elucidate a fundamental understanding of the role of materials architecture on device performance and to explore the utility of hierarchical nanostructures for 3D battery applications.

3.2 Summary and Forecast for Future

Despite the fact that nanostructuring of battery electrodes can increase battery power density, the 2D planar design fundamentally limits the amount of energy that can be stored and power that can be delivered per unit area, mass, and volume. 3D battery architectures exploit the advantages of nanostructuring, while potentially decreasing the areal footprint of a 2D design. In this task, we are pursuing a variety of potential three-dimensional designs that are generally composed of a 3D matrix of the electrodes (periodic or aperiodic) in order to maximize the number of interfaces and thus interfacial reactions in the battery. Although transport between the electrodes remains 1D, the additional interfaces that are interpenetrated in the 3D network offer major gains in the areal footprint, while the 3D design minimizes transport distances between and in the electrodes which can result in higher power densities. Here, we are developing the fabrication and processing methodologies for battery electrodes that can be implemented to coat 3D architectures with micron and nanosized features. Atomic layer deposition (ALD) is a gas phase self limiting growth technique that allows for uniform, conformal growth of thin films on 3D structures using sequential surface reactions. We have developed a low temperature ALD (LT-ALD) process in order to deposit conformal and uniform films of amorphous SnO_x on CNTs and a high temperature (HT-ALD) process to deposit nano particles of Sn and SnO. We have carried out morphological and electrochemical analysis to provide a detailed understanding of the complex architecture of the hybrid electrodes and how this relates to their device performance. We have demonstrated the capability to create distinctly different forms of the hybrid SnO_x-carbon anode material – either nanoparticles attached directly to the carbon nanotubes or as a conformal coating. The measured specific capacities of the SnO_x-Buckypaper composites are quite high and are considerably higher than graphite itself. Importantly, for small particle sizes, the specific capacity was shown to be greater than the theoretical capacity for Sn (Li_{4.4}Sn, 993 mAh/g) which suggests that nanosized particles of Sn have a larger solid solution range with lithium than bulk Sn particles. This observation could have important implications for designing even higher energy density systems. Furthermore, the area-specific capacity was shown to be >8 mAh/cm², which is over one order-of-magnitude higher than for thin film SnO₂ electrodes (0.2-0.8 mAh/cm²). This is a result of the thickness and high degree of surface area within the nanocomposite electrode film. It should be noted that the ability to achieve high areal capacities is a major goal for developing 3D electrodes and batteries. Besides showing the enhanced electrochemical performance that can be achieved by nanosizing electrode materials, these results demonstrate the importance of having free volume available when using high capacity anodes, which has implications in the designs of both traditional 2D and novel 3D batteries.

3.3 Task Introduction

First generation Li-ion batteries are based on a 2D planar design containing electrodes (a LiCoO₂ cathode and graphite anode) with micron and millimeter sized particles and a non-aqueous liquid electrolyte trapped within millimeter sized pores of a polypropylene separator.[1] These batteries are low power

devices because of the low intrinsic diffusivity of Li ions through the solid state electrodes. However, by decreasing particle size and nano structuring the electrodes, the rate of Li-ion insertion/removal can be increased because of the shorter Li-ion transport distances within the particles.[7] Correspondingly, electron transport can also be enhanced because of shorter electron transport distances.[7] The high surface area of nanoparticles also permits high contact area with the electrolyte and hence a higher lithium-ion flux across the interface compared to lower aspect ratio electrodes. Therefore, decreasing particle dimensions can increase the power density of Li ion batteries. [1]

Besides improved ion and electron transport, nano sized particles have several other advantages. They can undergo reactions that cannot take place in micron sized materials. For example, mesoporous β - MnO_2 can undergo reversible Li intercalation and maintain the rutile structure, while Li cannot electrochemically intercalate into micron sized β - $\text{MnO}_{2.3}$. For very small particles, the chemical potentials for Li ions and electrons may be modified, resulting in a change of the electrode potential. [9] The range of compositions over which solid solutions exist is often wider in nanoparticles, [10] and the strain associated with intercalation is also better accommodated in nano materials. [1]

Even though nano structuring electrodes can increase battery power density, the 2D planar design fundamentally limits the amount of energy that can be stored and power that can be delivered per unit area, mass, and volume. However, 3D battery architectures exploit the advantages of nano structuring, while decreasing the areal footprint of a 2D design. Three-dimensional designs are generally composed of a 3D matrix of the electrodes (periodic or aperiodic) to maximize the number of interfaces and thus interfacial reactions in the battery. [11] Although transport between the electrodes remains 1-D, the additional interfaces that are interpenetrated in the 3D network offer major gains in the areal footprint, while the 3D design minimizes transport distances between and in the electrodes which can result in higher power densities. [12]

Additionally, a completely solid state 3D design will allow for the replacement of highly volatile and flammable liquid electrolytes with a solid electrolyte. Liquid electrolytes are generally used in conventional batteries because of their inherently higher Li ion conductivity than their solid counterparts. However, the difference in the ionic conductivity can be mitigated in a 3D design by the shorter transport distances between electrodes and increased number of interfaces within the 3D network. Therefore, besides providing gains in energy and power density, solid state 3D architectures can improve safety and prevent the risk of electrolyte leakage.

3.4 Low Temperature ALD of SnO_x

Although 3D architectures are promising for improving battery performance, the challenge is building a 3D electrode network that contains a fully interconnected pore structure, and then conformally coating the walls of this structure with an electrolyte, while still allowing enough open void space to add the second electrode (cathode or anode). The void volume determines the internal architecture of the cell and is the most important design component for further structural modifications. Therefore, the fabrication of 3D electrodes and batteries is dependent on developing processing techniques that can be implemented to coat 3D architectures with micron and nanosized features.

Atomic layer deposition (ALD) is a gas phase self limiting growth technique that allows for uniform, conformal growth of thin films on 3D structures using sequential surface reactions. We have developed a low temperature ALD (LT-ALD) process in order to deposit conformal and uniform films of amorphous SnO_x on CNTs and a high temperature (HT-ALD) process to deposit nano particles of Sn and SnO . Tetrakis(dimethyl)amino tin (TDMASn) was used as the tin precursor in order to avoid corrosive halogenated precursors like SnCl_4 and SnI_4 , as well as, to prevent the formation of halogen impurities in the deposit.

The low temperature SnO_x ALD process deposits conformal uniform films on the surface multiwalled carbon nanotubes (MW-CNTs). Figure 17 shows representative TEM images of MW-CNTs after 100 and 300 TDMASn-H₂O ALD cycles. After 100 ALD cycles, a ~4 nm thick layer has been deposited on the surface of the carbon nano tubes (Figure 17A). The initial growth rate on the tubes during the first 100 cycles is ~0.4 Å/cycle. After 100 cycles, the growth rate increases to ~0.7 Å/cycle. The SnO_x growth rate is initially slower because of the limited reactivity of the carbon sp² surface of the MW-CNTs. Therefore, several exposures of water and TDMASn are required to initiate SnO_x growth on the CNTs. Figure 17B displays a TEM image of a MW-CNT after 300 ALD cycles. The tubes are conformally coated with an ~18.5 nm thick SnO_x coating.

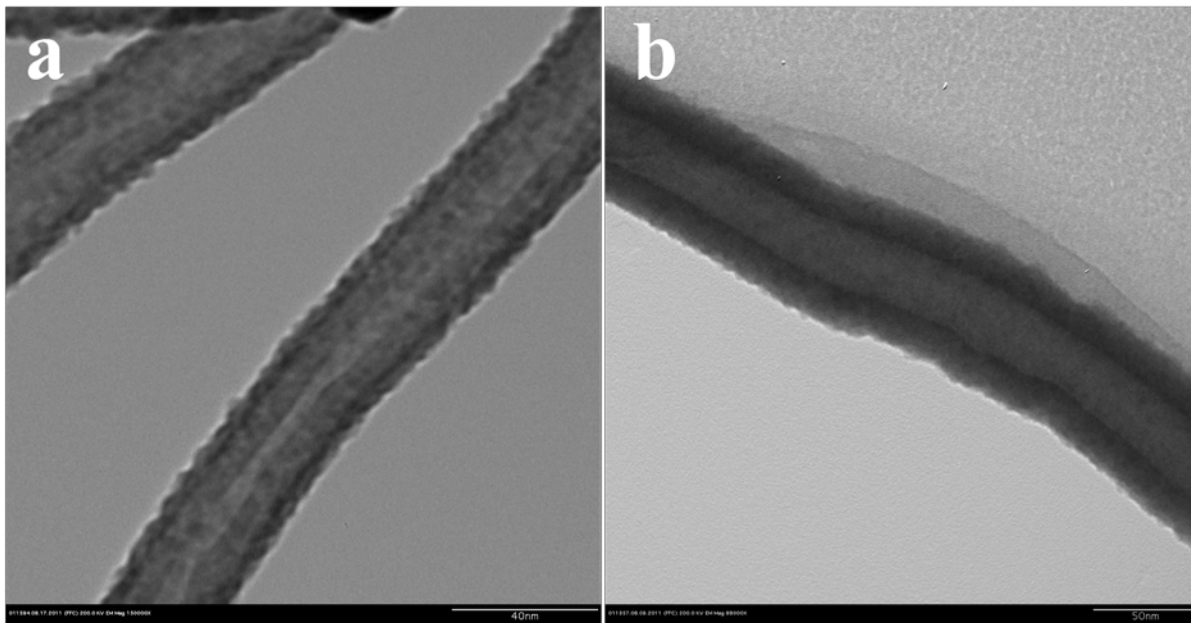


Figure 17. TEM images of (a) CNT coated with 100 LT-ALD cycles of SnO_x and (b) CNT coated with 300 LT-ALD cycles of SnO_x.

X-ray diffraction (XRD) patterns of MW-CNTs and as deposited SnO_x on MW-CNTs are shown in Figure 18. The MW-CNTs show a major peak at 26.4° consistent with the graphite (002) peak. Two smaller peaks are observed at 44° and 54.5° which correspond to the graphite (100) and (004) peaks. The decreasing intensity of the graphite peaks with greater number of ALD cycles is caused by the increase in thickness of SnO_x on the MW-CNTs. The as deposited SnO_x is amorphous and shows two broad peaks at 31° and 55°. Annealing the amorphous SnO_x / CNT samples in air converts the amorphous SnO_x to SnO₂. Figure 19 shows an XRD pattern of SnO_x coated CNTs after being annealed for 2 hours at 400°C. All of the peaks can be indexed to tetragonal SnO₂, PDF# 77-0450.

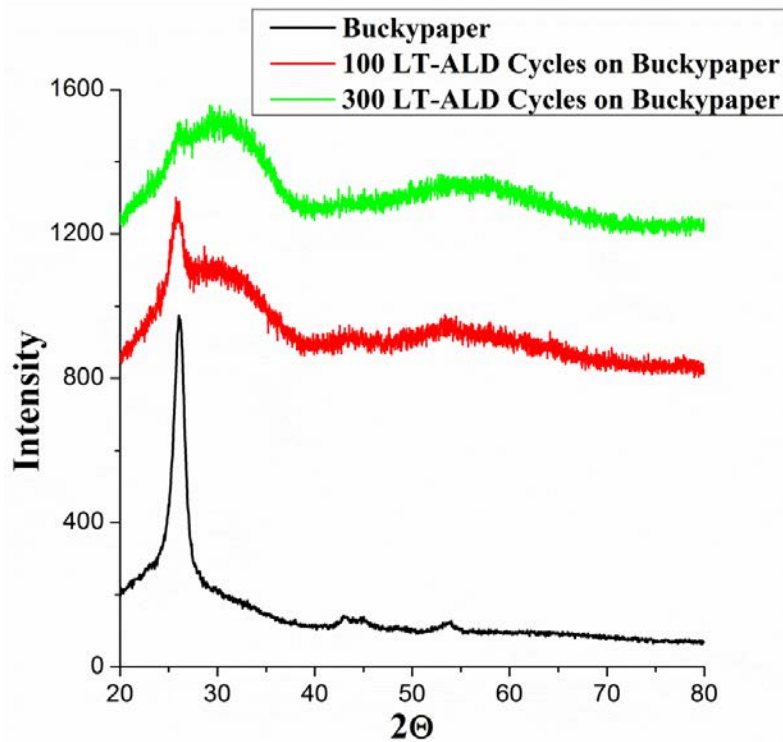


Figure 18. XRD patterns of CNTs, CNTs coated with 100 LT-ALD SnO_x cycles, and CNTs coated with 300 LT-ALD SnO_x cycles.

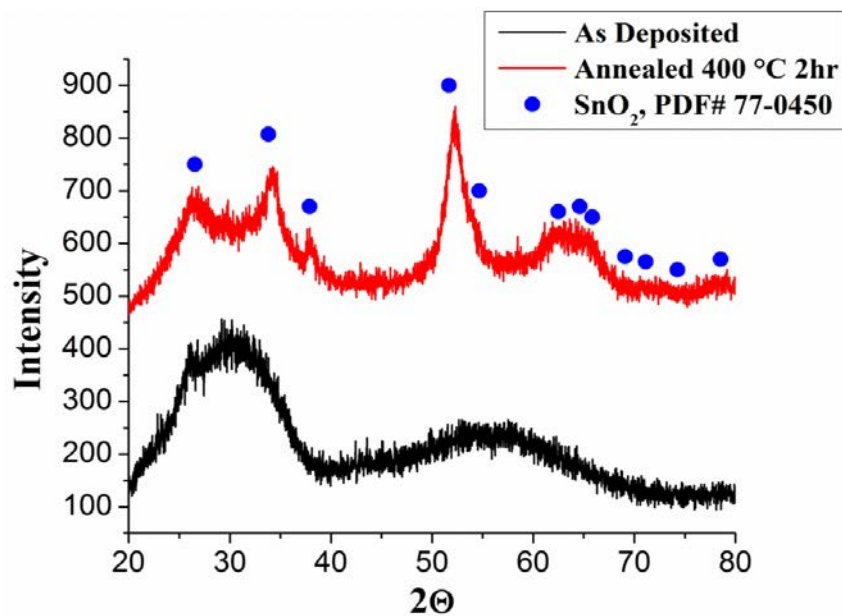


Figure 19. XRD patterns of LT-ALD as deposited SnO_x on CNTs and annealed SnO_x on CNTs.

3.5 High Temperature ALD of SnO_x

A high temperature SnO_x ALD (HT-ALD) process was developed in order to deposit nanoparticles of SnO_x on 3D architectures. Tin undergoes a large volume expansion (>300%) during lithiation which can lead to pulverization. By dispersing SnO_x nanoparticles on CNTs rather than depositing a conformal layer or micron sized particles, the SnO_x can be fully lithiated without volume constraints. The nanoparticles can then expand into the open volume during lithiation without fracturing. Also, nanosizing SnO_x can reduce the volumetric stresses within individual particles caused by lithiation.

Figure 20 shows representative top views of MW-CNT Buckypaper before SnO_x deposition and after 50, 100, 300, and 500 TDMASn-H₂O ALD cycles. The SnO_x ALD process initially deposited nanoparticles of Sn and SnO on the surface of the MW-CNT Buckypaper. Increasing the number of ALD cycles led to agglomeration of the particles and eventually conformal coverage on the top surface of the MW-CNT Buckypaper.

Figure 20a shows the Buckypaper which is composed of highly entwined MW-CNTs that range in diameter from 10 to 30 nm. Although the CNTs are densely packed, nanometer sized pores up to 100 nm wide can be observed in the 120 micron thick paper. Coating the Buckypaper with 50 ALD cycles (Figure 20b) resulted in 20 nm SnO_x particles well dispersed on the surface of the Buckypaper. After 100 ALD cycles, the 20 nm SnO_x particles are still present but are more densely packed and larger agglomerates have begun to form (Figure 20c).

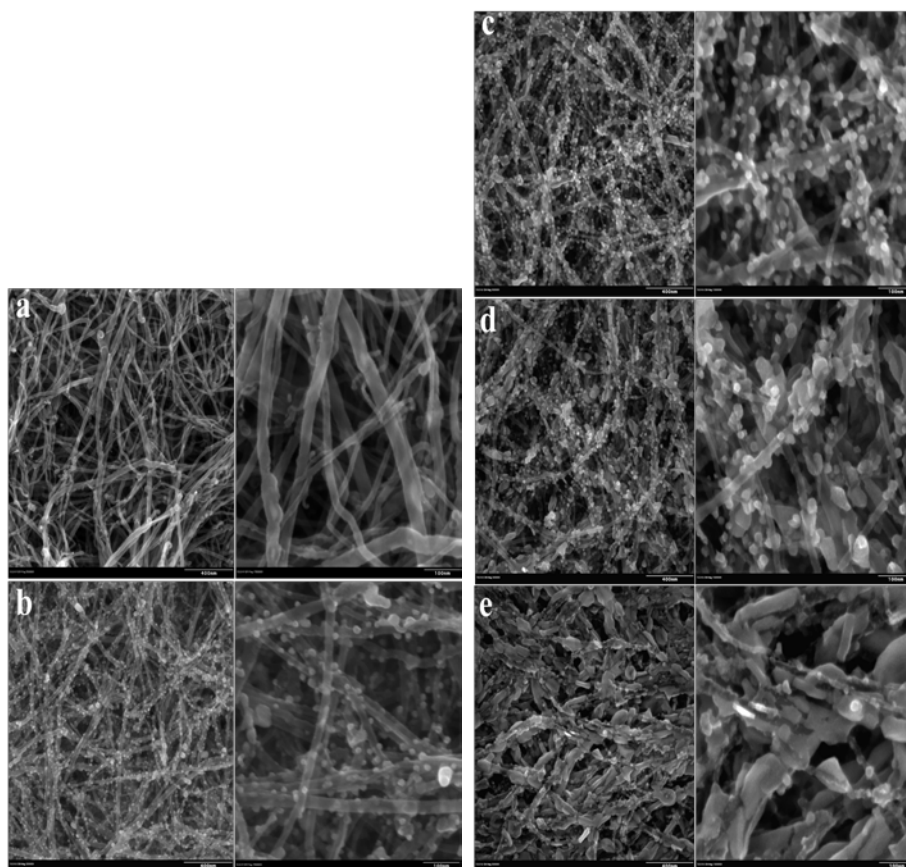


Figure 20. SEM images of (a) MW-CNT Buckypaper and SnO_x coated Buckypaper after (b) 50, (c) 100, (d) 300, (e) 500 TDMASn-H₂O HT-ALD cycles.

Increasing the number of TDMASn-H₂O ALD cycles increases the agglomeration and particle size. Buckypaper coated with 300 ALD cycles begins to show evidence of conformal deposition of SnO_x on the tubes and large (>100nm) agglomerate formation. Buckypaper with 500 ALD cycles can be seen in Figure 20e. A nearly complete conformal coating of SnO_x has formed on the surface of the Buckypaper CNTs. The nanoparticles have grown into large agglomerates that coat the entire length and diameter of the tubes.

X-ray diffraction patterns of MW-CNT Buckypaper and as deposited SnO_x on Buckypaper are shown in Figure 21a. The decreasing intensity of the graphite peaks with greater number of ALD cycles is caused by the increased surface coverage of the MW-CNTs with SnO_x. Consistent with the SEM images after 50 ALD cycles the majority of the surface of the CNTs is not covered with SnO_x, while after 500 ALD cycles the tubes are essentially conformally coated on the top surface. The as deposited SnO_x XRD patterns contain a mixture of Sn and SnO. All of the peaks were indexed to Sn (JCPDS PDF No. 04-0673) and SnO (JCPDS PDF No. 04-0673). The Sn:SnO ratio was dependent on the number of ALD cycles. Increasing the number of ALD cycles increased the relative amount of SnO to Sn.

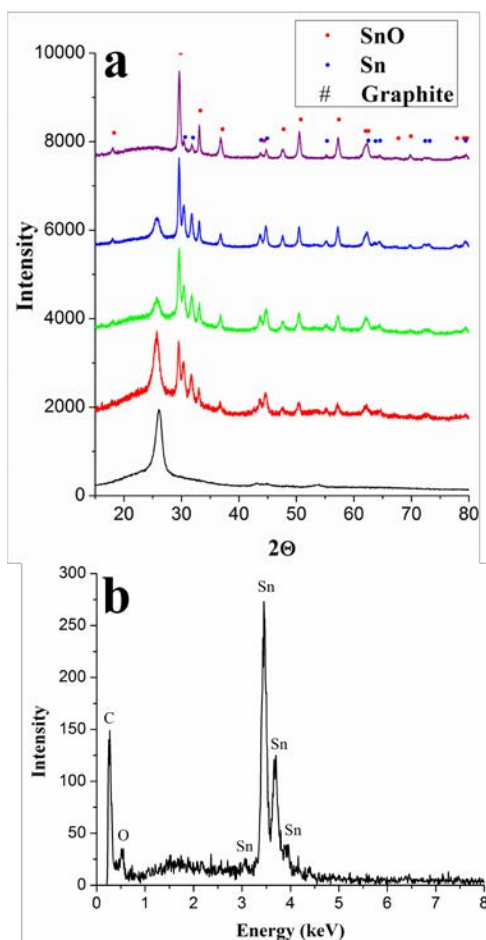


Figure 21. (a) XRD patterns of Buckypaper and SnO_x deposited on Buckypaper after (b) 50, (c) 100, (d) 300, (e) 500 TDMASn-H₂O HT-ALD cycles (b) a representative EDX spectra of Buckypaper coated with 300 SnO_x HT-ALD cycles.

Interestingly, there was no evidence of the presence of SnO₂ in the as deposited sample. Meng et al. recently reported depositing SnO₂ on nitrogen doped CNTs by ALD using a different tin precursor, SnCl₄. [13] The authors reported depositions performed at 200 and 300°C led to the growth of SnO₂. However, there is no evidence of SnO₂ present after our 250°C ALD process. The difference in phase formation can likely be explained by the different tin precursors and different growth conditions. Also, Meng et al. reported the presence of chloride in there as deposited SnO₂, [13] which is not surprising because of the chloride precursor. However, a representative EDX spectrum displayed in figure 21b of SnOx coated Buckypaper after 300 HT-ALD cycles shows no presence of impurities when TDMASn is used as the tin precursor.

The SnOx deposition is the most concentrated on the top surface of the Buckypaper; however, particles also grew uniformly throughout the inside of the Buckypaper. Figure 22 displays representative cross sectional SEM images from the middle of the SnOx ALD coated Buckypaper after 100 and 500 HT-ALD cycles. Despite the close packing of the tubes and the resulting limited porosity, the TDMASn and water penetrate all the way through the Buckypaper resulting in regularly dispersed SnOx nanoparticles. Initially, ~10 - 20nm particles form that are largely isolated from each other. With more cycles, the particles become more concentrated along the CNTs. Even after 500 TDMASn – H₂O ALD cycles, the deposits are primarily ~20nm particles. Larger agglomerates (~50 nm) have formed, but are significantly smaller than the agglomerates on the surface (Figure 4d and 4e). The SnOx nanoparticle deposition throughout the Buckypaper demonstrates that the ALD process developed is an effective method for coating 3D structures with SnOx nanoparticles. The nanoparticles are evenly dispersed throughout a highly tortuous 3D structure with limited porosity that is over 120 microns thick.

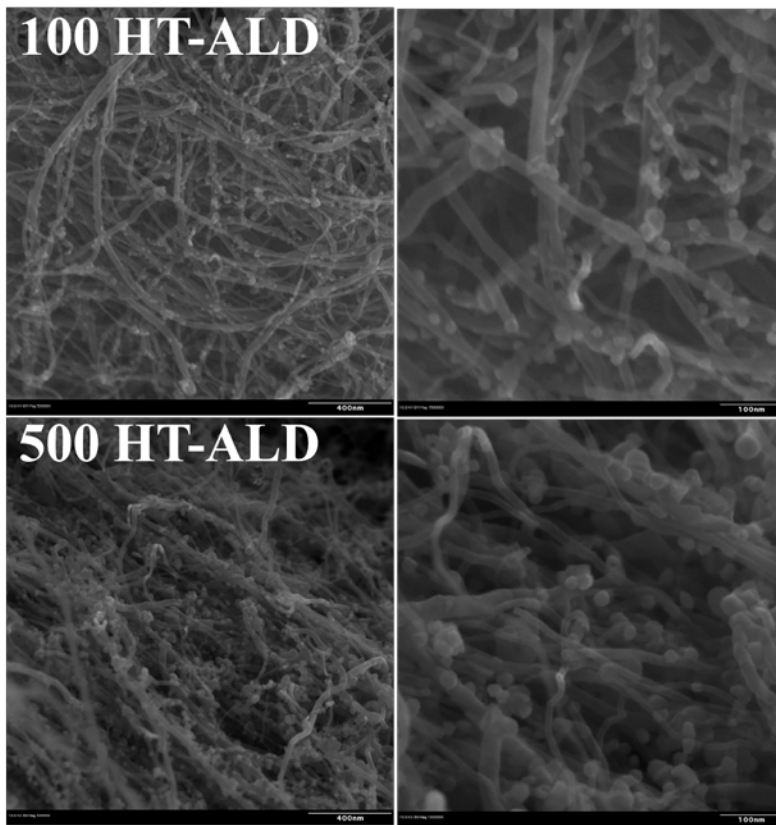


Figure 22. Cross sectional SEM images of SnO_x coated Buckypaper after 100 and 500 HT-ALD cycles.

Annealing the amorphous SnO_x coated MW-CNT Buckypaper converts the SnO and Sn particles to SnO₂. Figure 23 shows an XRD pattern of SnO_x coated CNTs before and after being annealed for 2 hours at 400°C. All of the peaks after annealing can be indexed to SnO₂, PDF# 29-1484, which has an orthorhombic unit cell. It should be noted that the low and high temperature ALD processes both result in the formation of SnO₂ after annealing; however, they also result in different SnO₂ crystal structures.

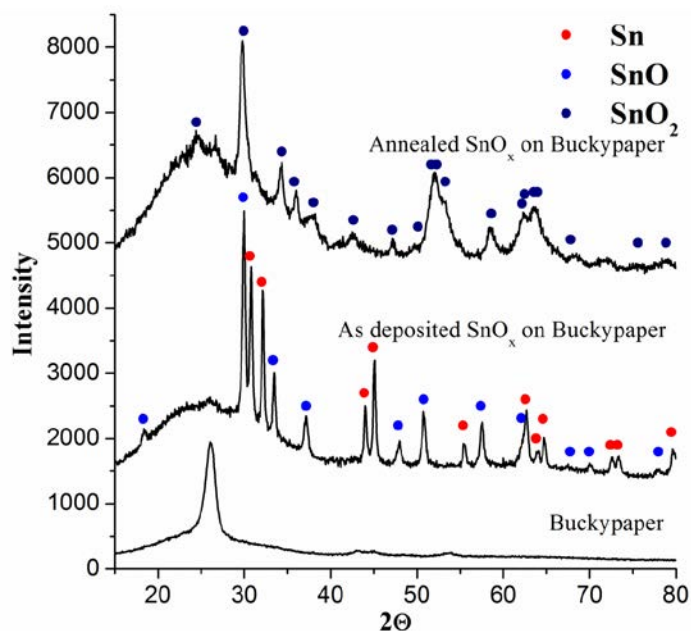


Figure 23. XRD patterns of Buckypaper, HT-ALD as deposited SnO_x on Buckypaper, and HT-ALD annealed SnO_x on Buckypaper.

3.6 SnO_x Nanoparticle Coated Buckypaper 3D Electrodes

Next generation Li ion batteries require higher storage capacities and increased energy densities. Traditional anodes like graphite are limited by their theoretical maximum specific capacity (372 mAh/g) as well as slow Li insertion rate which correspondingly limit battery energy and power densities. Metals and Metal oxides such as Sn and SnO₂ have higher specific capacities (993 and 782 mAh/g) compared to carbon and have shown improved rate capabilities as hybrid (SnO_x – C composites) anodes. However, Sn and SnO₂ have been limited by their large volume changes during Li alloying that leads to pulverization, and they have not been implemented into 3D electrodes.

Recently, it has been shown that nanosizing SnO_x can lead to improved cycling performance in SnO_x-C hybrid anodes. [14-19] Additionally, Buckypaper provides an effective 3D scaffold that we have demonstrated can be coated with high capacity SnO_x nanoparticles. Therefore, the SnO_x nanoparticle – Buckypaper composites were investigated as anodes for Li ion batteries. Buckypaper and SnO_x-Buckypaper composites were tested in a half cell design against lithium as the counter electrode without the addition of additives such as other forms of carbon or polymer binders. The lithium insertion/extraction was performed at a current density of 25 mA/g in the voltage range of 0.005 to 2.0V.

The initial discharge capacities were very high for all samples and can be explained by the irreversible decomposition of the electrolyte and formation of a solid electrolyte interface (SEI) layer on the surface

of the CNTs. Charge-discharge curves of uncoated Buckypaper and Buckypaper coated with 300 SnOx HT-ALD cycles are shown in Figure 24. The second, fifth, tenth, and fifteenth charge and discharge capacity curves for Buckypaper is shown in Figure 24a and the corresponding curves for the 300 SnOx ALD – Buckypaper sample are shown in Figure 24b. The uncoated Buckypaper sample had a discharge capacity of 225 during the second discharge cycle which faded and stabilized at 175 mAh/g. The 300 SnOx ALD – Buckypaper had a discharge capacity of ~690 mAh/g during the second discharge cycle which faded to 575 mAh/g by the fifteenth discharge cycle. The 300 SnOx ALD – Buckypaper discharge curves showed two major plateaus at ~0.7V and ~0.4V which is expected for the lithiation of tin.[20] The plateaus are not observed in the uncoated Buckypaper electrode and confirms that the high capacity of the SnOx ALD coated electrodes is due to the presence of tin.

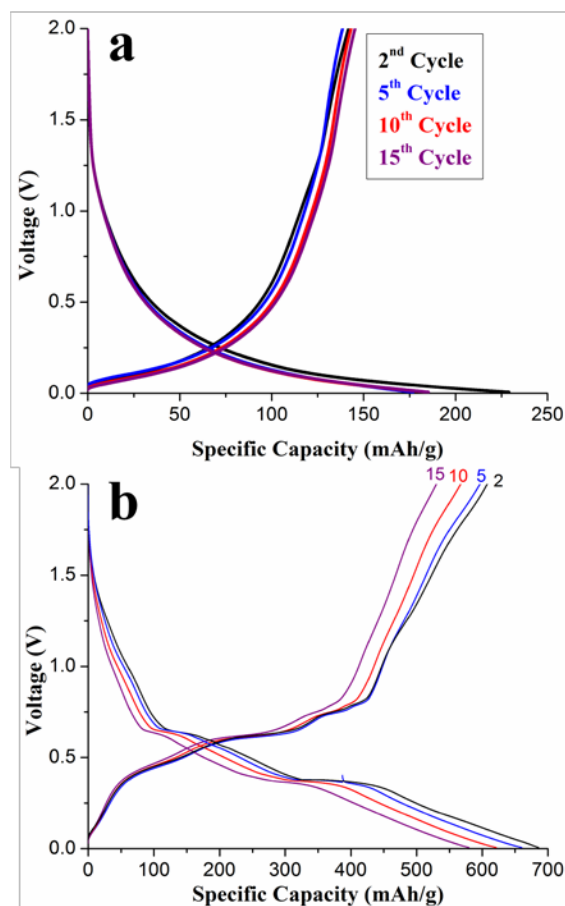


Figure 24. (a) Charge-discharge curves of Buckypaper and (b) charge-discharge curves of Buckypaper coated with 300 SnO_x HT-ALD cycles cycled against Li.

The specific discharge capacities of the non-coated Buckypaper and SnO_x-Buckypaper composites with different number of HT-ALD cycles are shown in Figure 25a. It is important to note that the capacities were calculated based on the total mass of the Buckypaper and SnO_x, and there were no additives such as polymer binders (i.e. PVDF) or conductive carbon added to the electrodes. All of the SnO_x coated Buckypaper composites have significantly higher capacities than the uncoated Buckypaper. Increasing the Sn loading in the samples increases the capacity because Sn has a higher maximum theoretical capacity than carbon. However, after ~300 ALD cycles the capacity begins to plateau which is a result of the saturation of the Buckypaper with SnO_x. Within the Buckypaper there is limited remaining uncoated

surface area on the CNTs after 300 HT-SnO_x cycles; therefore, a thicker deposit begins forming on the surface (Figure 20e) and the capacity plateaus.

The specific capacity of the SnO_x-Buckypaper composites are quite high and are considerably higher than graphite (theoretical capacity 372 mAh/g). The composite anodes faded at a rate of ~2% per cycle, which is significantly slower than the fading reported for SnO₂-C bulk powders. The fade rate could also be decreased by decreasing the charge and discharge rates.

The specific capacity of the SnO_x component of the hybrid anodes was also calculated and is displayed in figure 25b. The specific capacity of the Buckypaper was subtracted from the SnO_x-Buckypaper composite electrodes and then the specific capacity was recalculated using the mass of the SnO_x deposit. Based on the specific capacity of the SnO_x component, the SnO_x in the 50 SnO_x HT-ALD coated Buckypaper had the highest specific capacity. The 50 SnO_x HT-ALD coated Buckypaper is comprised of small isolated particles on the surface which allow for all of the Sn to participate in the lithiation process. The specific capacity is also greater than the theoretical capacity for Sn (Li_{4.4}Sn, 993 mAh/g) which suggests that nanosized particles of Sn have a larger solid solution range with lithium than bulk Sn particles. Increasing the number of ALD cycles causes the particle size to increase as well as agglomeration. The SnO_x in the 500 SnO_x HT-ALD coated Buckypaper has the largest particles and contains the most agglomerates. It also has the lowest capacity. The capacity is less than the theoretical capacities of Sn and SnO (884 mAh/g). The lower capacities indicate that SnO_x in the 500 SnO_x HT-ALD Buckypaper electrode is behaving like a bulk powder, which is consistent with the larger particle size. The lower than theoretical capacity values also suggests that fracturing occurs in the first charge-discharge cycles and all of the Sn is not being fully lithiated during discharging.

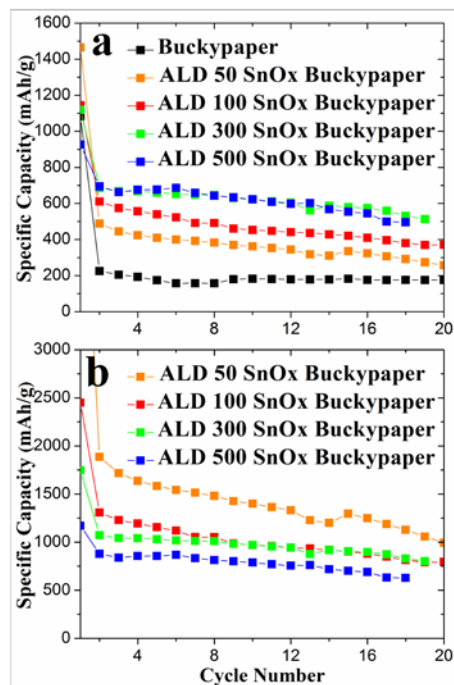


Figure 25. (a) Specific capacity of the Buckypaper and SnO_x coated Buckypaper with different number of HT-ALD cycles (b) Specific capacity of the SnO_x component of the HT-ALD SnO_x coated Buckypaper.

The areal charge-discharge capacities for the 300 SnO_x HT-ALD cycle Buckypaper composite is shown in Figure 26. The areal capacity is >8 mAh/cm², which is over a magnitude higher capacity than thin film SnO₂ electrodes (0.2-0.8 mAh/cm²). [21-22] The high areal capacity is a result of the thickness and large amount of surface area within the Buckypaper that has been coated with SnO_x nanoparticles. The ability to achieve high areal capacities is a major goal for developing 3D electrodes and batteries. Figure 26 shows that 3D electrodes can attain high areal capacities, while also demonstrating the utility of the SnO_x ALD process we have developed for coating complex 3D structures.

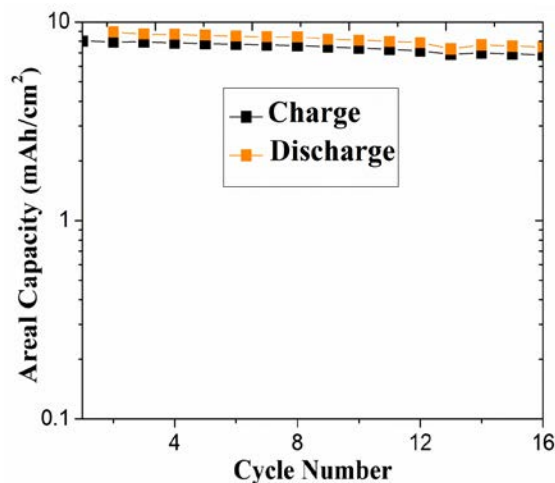


Figure 26. Areal charge and discharge capacities of Buckypaper coated with 300 SnO_x HT-ALD cycles.

3.7 Electrochemical Performance of Conformal Growth vs. Nanoparticles

High volume expansion anode materials have been reported to have improved electrochemical properties when they are nanosized. Although improved electrochemical performance has been reported, there are no reports on the difference in performance comparing conformal coverage of nanometer thick thin films and disperse nano particle. Therefore, we investigated the performance of SnO_x on MW-CNT Buckypaper samples that were conformally coated with SnO_x (LT-ALD) and coated with SnO_x nanoparticles (HT-ALD). The difference in coating resulted in dramatically different results when cycled against lithium. The SnO_x-Buckypaper composites were cycled as deposited. Therefore, the composites consisted of Buckypaper was a conformal coating of amorphous SnO_x and Buckypaper coated with Sn and SnO nanoparticles. Figure 27 shows top down SEM images of SnO_x coated Buckypaper prepared using the LT-ALD and HT-ALD processes. The deposit is the most concentrated on the top surface. However, the MW-CNTs are deposited throughout the 120 μm thick paper.

Figure 28 displays the discharge capacities and coulombic efficiencies of Buckypaper coated with 100 SnO_x ALD cycles. The first cycle for both electrodes was high owing to the formation of the irreversible SEI layer. Disregarding the capacity of the first cycle, the capacity of the nanoparticle Buckypaper electrode faded at a rate of ~2% and the coulombic efficiency was maintained around 90%. The initial discharge capacity was ~600 mAh/g and after the 20th cycle the capacity was still >400 mAh/g. However, the capacity of the conformally coated sample decreased at a significantly faster rate. The second discharge capacity was only 500 mAh/g and by the 10th cycle the capacity was below 200 mAh/g. The lower capacity of the conformally coated MW-CNT paper is due to the large volume changes during cycling. There is limited free volume in the conformally coated SnO_x-Buckypaper electrode. Therefore, when the SnO_x expands during lithiation, the conformal coating fractures. Particles that are fractured

come unattached from the CNTs and no longer participate in lithiation. After several cycles, very little of the SnO_x is still in contact with the CNTs and still participating in the lithiation process. The discharge capacity of the conformally coated samples is ~200 mAh/g after ten charge-discharge cycles, which is the same as the uncoated Buckypaper in Figure 25A. Thus, confirming that the SnO_x is no longer contributing significantly to the capacity.

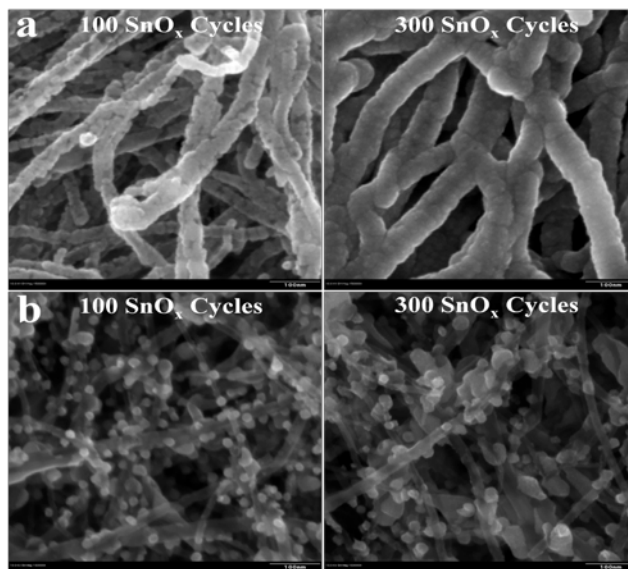


Figure 27. (a) LT-ALD of SnO_x on Buckypaper (b) HT-ALD of SnO_x on Buckypaper.

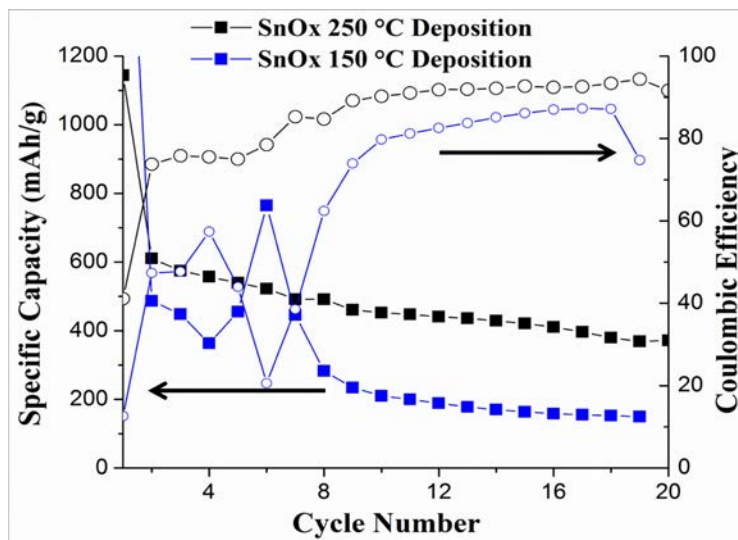


Figure 28. Specific capacity and coulombic efficiency of Buckypaper coated with 100 SnO_x ALD cycles. The squares correspond with the specific capacity and the circles with the coulombic efficiency.

The discharge capacities of Buckypaper coated with 300 SnO_x ALD cycles are shown in Figure 29. The capacity of the 300 SnO_x LT-ALD decreased at a much faster rate than the 100 SnO_x-Buckypaper LT-ALD composite. The faster rate of degradation is caused by the thicker conformal SnO_x coating on the MW-CNT Buckypaper. TEM showed that the thickness of amorphous SnO_x after 100 LT-ALD cycles was 4 nm, while after 300 LT-ALD cycles an 18.5 nm thick coating is present (Figure 17). The thicker coating results in more rapid degradation until the paper stops cycling as an electrode. The large expansion of the SnO_x during lithiation in the limited free volume of the Buckypaper led to the destruction of the electrode. The SnO_x expanded so much that it caused the Buckypaper to break apart and the MW-CNTs to lose electrical contact.

The SnO_x nanoparticle coated Buckypaper retained their capacity significantly better than the conformally coated SnO_x-Buckypaper. The improved cycling performance of the nanoparticles compared to the conformal coatings provides direct evidence that reducing particle size can enhance electrochemical performance. Although the coatings were between 4 and 18.5 nm thick, the SnO_x essentially behaved as a large thin single particle that was coating the MW-CNTs and pulverized during cycling. Also, the cycling performance of the conformally coated Buckypaper was poor because the anode needs to be able to expand in three dimensions during the lithiation; however, since a conformal film was on the tubes there was no open volume for expansion in the plane of the coating. Besides showing the enhanced electrochemical performance that can be achieved by nanosizing electrode materials, these results demonstrate the importance of having free volume available when using high capacity anodes, which has implications in the designs of both traditional 2D and novel 3D batteries.

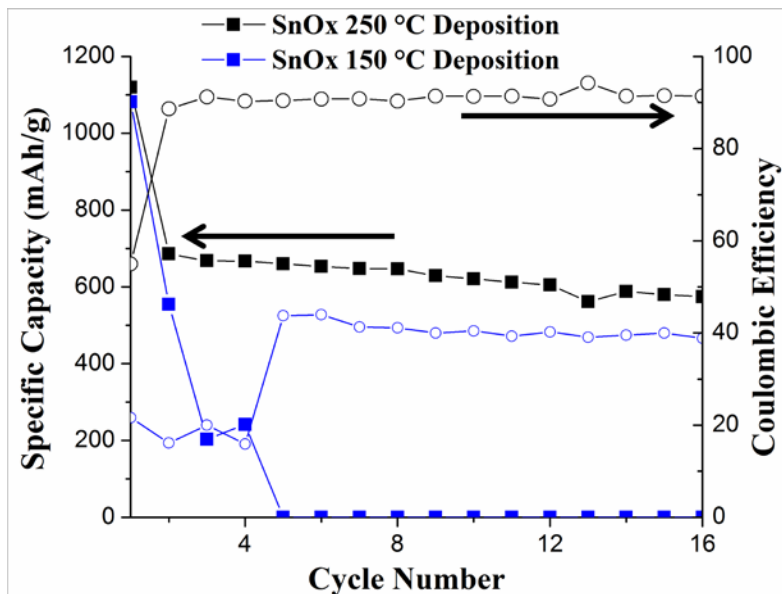


Figure 29. Specific capacity and coulombic efficiency of Buckypaper coated with 300 SnO_x ALD cycles. The squares correspond with the specific capacity and the circles with the coulombic efficiency.

4 RELATED PUBLICATIONS

Below is a listing of publications prepared and presented under the Electrochemical Energy Storage Materials Work Unit. These publications present a much more detailed technical description of all of the work conducted under the effort.

Rao, R., Liptak, D., Cherukuri, T., Yakobson, B. and Maruyama, B., “ In situ evidence for chirality-dependent growth rates of individual carbon nanotubes.” *Nature Materials*, Vol., 11, 3, pp. 213-216, 2012.

R. Rahul Rao, J. Reppert, R. Podila, X. Zhang, A. M. Rao, S. Talapatra and B. Maruyama, “Double resonance Raman study of disorder in CVD-grown single-walled carbon nanotubes.” *Carbon*, Volume 49, Issue 4, April 2011, Pages 1318-1325.

Perea-Lopez, N., Rebollo-Plata, B., Briones-Leon, J., Morelos-Gomez, A, Hernandez-Cruz, D., Hirata, G.A., Meunier, V., Botello-Mendez, A.R., Charlier, J-C., Maruyama, B., Munoz-Sandoval, E. Lopez-Urias, F., Terrones, M., and Terrones, H. “Millimeter-Long Carbon Nanotubes: Outstanding Electron-Emitting Sources.” *ACS Nano*, 2011, 5 (6), pp 5072–5077.

R. Rao, N. Pierce, X. Zhang, R. Wheeler, B. Maruyama and S. Talapatra,” Understanding the Role of Sulfur in Tuning the Diameter and Morphology in the CVD Growth of Carbon Nanotubes.” *Materials Express*, Vol. 1, No. 2, June 2011 , pp. 160-166(7).

Kim, SM, Pint, CL, Amama, PB, Hauge, RH, Maruyama, B, Stach, EA, “Catalyst and catalyst support morphology evolution in single-walled carbon nanotube supergrowth: Growth deceleration and termination.” *Invited submission, J. Materials Research*, V. 25 (10) pp. 1875-1885, Oct. 2010

Rao, R, Eyink, KG, Maruyama, B, “Single-walled carbon nanotube growth from liquid gallium and indium.” *Carbon*, V. 48, (13) pp. 3971-3973, Nov. 2010.

Drummy, LF, Apt, S, Shiffler, D, Golby, K, LaCour, M, Maruyama, B, Vaia, RA, “Nanostructural evolution during emission of CsI-coated carbon fiber Cathodes.” *J. Appl. Phys.* V. 107 (11) 1 Jun 2010.

Kim, SM, Pint, CL, Amama, PB, Zakharov, DN, Hauge, RH, Maruyama, B, Stach, EA, “Evolution in Catalyst Morphology Leads to Carbon Nanotube Growth Termination.” *J. Phys. Chem. Lett.*, V. 1 (6), pp. 918-922, 18 Mar. 2010.

Amama, PB, Pint, CL, Kim, SM, McJilton, L, Eyink, KG, Stach, EA, Hauge, RH, Maruyama, B, “Influence of Alumina Type on the Evolution and Activity of, Alumina-Supported Fe Catalysts in Single-Walled Carbon Nanotube Carpet, Growth.” *ACS Nano*, V.4 (2) pp. 895-904, Feb 2010.

Akdim, B, Kim, SN, Naik, RR, Maruyama, B, Pender, MJ, Pachter, R, “Understanding effects of molecular adsorption at a single-wall boron, nitride nanotube interface from density functional theory calculations.” *Nanotechnology*, Vol 20, (35) 8 page, 12 Aug. 2009.

Amama, PB, Pint, CL, McJilton, L, Kim, SM, Stach, EA, Murray, PT, Hauge, RH, Maruyama, B, “Role of Water in Super Growth of Single-Walled Carbon Nanotube Carpets.” *Nano Letters*, Vo., 9 (1) pp. 44-49., Jan 2009.

Maruyama, B, Arepalli, S, Guest Editors, "The Proceedings of the Second Workshop on SWCNT Growth Mechanisms, Organized by NASA-JSC and Rice University." *J. Nanoscience and Nanotechnology*, V. 8, Nov. 2008.

Nicholas M. Bedford, Matthew B. Dickerson, Lawrence F. Drummy, Hilmar Koerner, Kristi M. Singh, Michael F. Durstock, Rajesh R. Naik, Andrew J. Steckl, *Advanced Energy Materials*, 2012, published online, DOI: 10.1002/aenm.201100674, "Nanofiber-Based Bulk-Heterojunction Organic Solar Cells Using Coaxial Electrospinning."

James R. Deneault, Xiaoyin Xiao, Tae-Sik Kang, Joanna S. Wang, Chien M. Wai, Gail J. Brown, Michael F. Durstock, *Journal of Chemical Physics and Physical Chemistry*, 2012, 13, 256-260, "Free-Standing Arrays of Isolated TiO₂ Nanotubes through Supercritical Fluid Drying."

Daniel T. Welna, Liangti Qu, Barney E. Taylor, Liming Dai, Michael F. Durstock, *Journal of Power Sources*, 2011, 196, 1455-1460, "Vertically aligned carbon nanotube electrodes for lithium ion batteries."

John D. Berrigan, Tae-Sik Kang, Ye Cai, James R. Deneault, Michael F. Durstock, Kenneth H. Sandhage, *Advanced Functional Materials*, 2011, 21(9), 1693-1700, "Protein enabled layer-by-layer syntheses of aligned, porous-wall, high-aspect-ratio TiO₂ nanotube arrays." (Cover Article)

Gerard K. Simon, Benji Maruyama, Michael F. Durstock, David J. Burton, Tarun Goswami, *Journal of Power Sources*, 2011, 196, 10254-10257, "Silicon-Coated Carbon Nanofiber Hierarchical Nanostructures for Improved Lithium-Ion Battery Anodes."

Maxim N. Tchoul, Scott P. Fillery, Hilmar Koerner, Lawrence F. Drummy, Folusho T. Oyerokun, Peter A. Mirau, Michael F. Durstock and Richard A. Vaia, *Chemistry of Materials* 2010, 22(5), 1749-1759, "Assemblies of titanium dioxide-polystyrene hybrid nanoparticles for dielectric applications."

Kuanping Gong, Feng Du, Zhenhai Xia, Michael Durstock, Liming Dai, *Science*, 2009, 323, 760-764, "Nitrogen doped carbon nanotube arrays with high electrocatalytic activity for oxygen reduction."

Zongwu Bai, Mitra Yoonessi, Shane B. Juhl, Lawrence F. Drummy, Michael F. Durstock, Thuy D. Dang, *Macromolecules* 2008, 41, 9483-9486, "Synthesis and Characterization of Multiblock sulfonated poly(arylenethioethersulfone) copolymers for proton exchange membranes".

Bai, Zongwu; Price, Gary E.; Yoonessi, Mitra; Juhl, Shane B.; Durstock, Michael F.; Dang, Thuy D. *Journal of Membrane Science* 2007, 305(1+2), 69-76, "Proton exchange membranes based on sulfonated polyarylenethioethersulfone and sulfonated polybenzimidazole for fuel cell applications".

Bai, Zongwu; Durstock, Michael F.; Rodrigues, Stanley J.; Reitz, Thom L.; Dang, Thuy D. *Polyimides and Other High Temperature Polymers* 2007, 4, 365-391, "Highly sulfonated poly(arylenethioethersulfone)s as proton-exchange membranes (PEMs) for fuel cells: Synthesis, characterization and performance".

Bai, Zongwu; Yoonessi, Mitra; Juhl, Shane B.; Drummy, Lawrence F.; Koerner, Hilmar; Durstock, Michael F.; Dang, Thuy D. *Polymer Preprints ACS National Meeting*, Chicago, IL, March, 2007, "Synthesis and Characterization of Segmented Multiblock Sulfonated Polyarylenethioethersulfones for Proton Exchange Membranes".

Bai, Zongwu; Yoonessi, Mitra; Durstock, Michael F.; Dang, Thuy D. PMSE Preprints (2007), 97 456-457, "Crosslinked polymer composites as proton exchange membrane (PEM) materials in fuel cell applications".

Venkatasubramanian, N.; Stricker, Jeffery T.; Durstock, Michael F.; Dang, Thuy D.; Wiacek, Kevin J.; Fries-Carr, Sandra Polymer Preprints (2007), 48(2), 290-291, "Self-healing phenomenon during the electrical breakdown of a spin-coated polyester dielectric".

Bai, Zongwu; Yoonessi, Mitra; Juhl, Shane B.; Drummy, Lawrence F.; Koerner, Hilmar; Durstock, Michael F.; Dang, Thuy D. Polymer Preprints (2007), 48(1), 508-509, "Synthesis and characterization of segmented multiblock sulfonated polyarylenethioethersulfones for proton exchange membranes".

Bai, Zongwu; Durstock, Michael F.; Dang, Thuy D. Journal of Membrane Science 2006, 281, 508-516, "Proton conductivity and properties of sulfonated polyarylenethioether sulfones as proton exchange membranes in fuel cells".

5 RECOMMENDATIONS

In-house research in electrochemical energy storage materials is planned in FY12 and the out years under the new work unit titled Nanostructured and Biological Materials In-House Research. Research will be focused to lead toward the realization of true 3D electrochemical energy storage materials to greatly improve power density, energy density, and lifetime to meet future Air Force energy needs. In addition, work will be focused on creating hybrid materials coupling photovoltaic energy harvesting with energy storage and structural properties to produce true off grid 24/7 energy availability for Air Force RPA, tents, airfield operations, and war fighters.

6 REFERENCES

1. Bruce, P.G., B. Scrosati, and J.M. Tarascon, *Nanomaterials for rechargeable lithium batteries*. Angewandte Chemie-International Edition, 2008. **47**(16): p. 2930-2946.
2. Zhang, H.G., X.D. Yu, and P.V. Braun, *Three-dimensional bicontinuous ultrafast-charge and -discharge bulk battery electrodes*. Nature Nanotechnology, 2011. **6**(5): p. 277-281.
3. Djenizian, T., I. Hanzu, and P. Knauth, *Nanostructured negative electrodes based on titania for Li-ion microbatteries*. Journal of Materials Chemistry, 2011. **21**(27): p. 9925-9937.
4. Yang, Z.G., et al., *Nanostructures and lithium electrochemical reactivity of lithium titanates and titanium oxides: A review*. Journal of Power Sources, 2009. **192**(2): p. 588-598.
5. Oudenhoven, J.F.M., L. Baggetto, and P.H.L. Notten, *All-Solid-State Lithium-Ion Microbatteries: A Review of Various Three-Dimensional Concepts*. Advanced Energy Materials, 2011. **1**(1): p. 10-33.
6. Park, M., et al., *A review of conduction phenomena in Li-ion batteries*. Journal of Power Sources, 2010. **195**(24): p. 7904-7929.
7. Arico, A. S.; Bruce, P.; Scrosati, B.; Tarascon, J.-M.; van Schalkwijk, W. Nat Mater 2005, 4, 366.
8. Jiao, F.; Bruce, P. Advanced Materials 2007, 19, 657.
9. Balaya, P.; Bhattacharyya, A. J.; Jamnik, J.; Zhukovskii, Y. F.; Kotomin, E. A.; Maier, J. Journal of Power Sources 2006, 159, 171.
10. Meethong, N.; Huang, H.-Y. S.; Carter, W. C.; Chiang, Y.-M. Electrochemical and Solid-State Letters 2007, 10, A134.
11. Long, J. W.; Dunn, B.; Rolison, D. R.; White, H. S. Chemical Reviews 2004, 104, 4463
12. Rolison, D. R.; Long, J. W.; Lytle, J. C.; Fischer, A. E.; Rhodes, C. P.; McEvoy, T. M.; Bourg, M. E.; Lubers, A. M. Chemical Society Reviews 2009, 38, 226.
13. Meng, X. B.; Zhong, Y.; Sun, Y. F.; Banis, M. N.; Li, R. Y.; Sun, X. L. Carbon 2011, 49, 1133.
14. Wen, Z. H.; Wang, Q.; Zhang, Q.; Li, J. H. Advanced Functional Materials 2007, 17, 2772.
15. Derrien, G.; Hassoun, J.; Panero, S.; Scrosati, B. Advanced Materials 2007, 19, 2336.
16. Hassoun, J.; Derrien, G.; Panero, S.; Scrosati, B. Advanced Materials 2008, 20, 3169.

17. Zhang, H. X.; Feng, C.; Zhai, Y. C.; Jiang, K. L.; Li, Q. Q.; Fan, S. S. *Advanced Materials* 2009, 21, 2299.
18. Paek, S. M.; Yoo, E.; Honma, I. *Nano Letters* 2009, 9, 72.
19. Wang, D. H.; Kou, R.; Choi, D.; Yang, Z. G.; Nie, Z. M.; Li, J.; Saraf, L. V.; Hu, D. H.; Zhang, J. G.; Graff, G. L.; Liu, J.; Pope, M. A.; Aksay, I. A. *Acs Nano* 2010, 4, 1587.
20. Courtney, I. A.; Dahn, J. R. *Journal of The Electrochemical Society* 1997, 144, 2045.
21. Lee, W. H.; Son, H. C.; Moon, H. S.; Kim, Y. I.; Sung, S. H.; Kim, J. Y.; Lee, J. G.; Park, J. W. *Journal of Power Sources* 2000, 89, 102.
22. Song, J.; Cai, M.-Z.; Dong, Q.-F.; Zheng, M.-S.; Wu, Q.-H.; Wu, S.-T. *Electrochimica Acta* 2009, 54, 2748.

LIST OF ACRONYMS, ABBREVIATIONS, AND SYMBOLS

ACRONYM	DESCRIPTION
°	degrees
1D	one dimensional
1M	one Molar
2D	two dimensional
24/7	24 hours per day, 7 days a week
3D	three dimensional
AFOSR	Air Force Office of Scientific Research
AFRL	Air Force Research Laboratory
ALD	Atomic Layer Deposition
CNT	Carbon Nanotube
Co	Cobalt
CO ₂	Carbon Dioxide
Cu	Copper
DEC	diethyl carbonate
DI	Deionized
EC	ethylene carbonate
EDS	Energy-dispersive X-ray spectroscopy
gm	gram
H	hour
H ₂ O	Water
HT-ALD	High Temperature Atomic Layer Deposition
La	Lanthium
Li	Lithium
Li-ion	Lithium ion
LiO ₂	Lithium Dioxide
LiO _x	Lithium Oxide (non stoichiometric)
LiPF ₆	lithium hexafluorophosphate
LT-ALD	Low Temperature Atomic Layer Deposition
Mn	Manganese
MWCNTs	Multiwalled Carbon Nanotubes
N ₂	Nydrogen
NaOH	Sodium Hydroxide
Ni	Nickel
nm	nanometer
mAh	milliamp hour
O	Oxygen
PAAM	porous anodic aluminum oxide membranes
PEG	polyethylene glycol
PS	Polystyrene Spheres
RPA	Remotely Piloted Aircraft
s	seconds
S	Siemens

SAD	selected area diffraction
sccm	standard cubic centimeter per minute
SEI	solid electrolyte interphase
SEM	Scanning Electron Microscope
Sn	Tin
SnO _x	Tin Oxide (non stoichiometric)
TDMASn	tetrakis-dimethylamino tin
TDMAT	tetrakis-dimethylamino titanium
TEM	Transmission Electron Microscope
Ti	Titanium
TiO ₂	Titanium Dioxide
TiO _x	Titanium Oxide (non stoichiometric)
USAF	United States Air Force
V	volts
VACNTs	Vertically Aligned Carbon Nanotubes
XRD	X-Ray Diffraction